Monitoring Physiological Signals Using Camera

by

Dangdang Shao

A Dissertation Presented in Partial Fulfillment
of the Requirements for the Degree
Doctor of Philosophy

Approved August 2016 by the
Graduate Supervisory Committee:

Nongjian Tao, Chair
Baoxin Li
Eric Hekler
Lina Karam

ARIZONA STATE UNIVERSITY

December 2016

ABSTRACT

Monitoring vital physiological signals, such as heart rate, blood pressure and breathing pattern, are basic requirements in the diagnosis and management of various diseases. Traditionally, these signals are measured only in hospital and clinical settings. An important recent trend is the development of portable devices for tracking these physiological signals non-invasively by using optical methods. These portable devices, when combined with cell phones, tablets or other mobile devices, provide a new opportunity for everyone to monitor one's vital signs out of clinic.

This thesis work develops camera-based systems and algorithms to monitor several physiological waveforms and parameters, without having to bring the sensors in contact with a subject. Based on skin color change, photoplethysmogram (PPG) waveform is recorded, from which heart rate and pulse transit time are obtained. Using a dual-wavelength illumination and triggered camera control system, blood oxygen saturation level is captured. By monitoring shoulder movement using differential imaging processing method, respiratory information is acquired, including breathing rate and breathing volume. Ballistocardiogram (BCG) is obtained based on facial feature detection and motion tracking. Blood pressure is further calculated from simultaneously recorded PPG and BCG, based on the time difference between these two waveforms.

The developed methods have been validated by comparisons against reference devices and through pilot studies. All of the aforementioned measurements are conducted without any physical contact between sensors and subjects. The work presented herein provides alternative solutions to track one's health and wellness under normal living condition.

DEDICATION

To my family.

ACKNOWLEDGMENTS

I would like to thank my advisor Dr. Nongjian Tao for his continued guidance, encouragement and support for my past few years. Not only did I gain knowledge under Dr. Tao, but I also learned to find and solve important problems, and to always have the big picture in mind.

I would like to thank the other members of my committee, Dr. Baoxin Li, Dr. Eric Hekler and Dr. Lina Karam, for their advice and precious discussions in the past few years.

It has been such a valuable experience to work at the Center for Bioelectronics and Biosensors, where I got the opportunity to learn from everyone in the group. A special thanks to Dr. Francis Tsow for leading me into the biomedical engineering field and helping me with the research. His mentorship has been very valuable to me. Thanks to Drs Chenbin Liu, Xiaonan Shan, and Wei Wang for the good advice. I would also like to thank Drs Erica Forzani, Shaopeng Wang, Fang Chen, Xiaojun Xian, Xincai Qin, Shaoyin Guo, Linliang Yin, and Xiulan Li, as well as Shan Chen, Hui Wang, Yue Deng, and Jingjing Yu.

I would also like to thank other researchers who have selflessly provided me help and guidance in my research: Drs Frank Marcus, Adam Hoover, and Kandala Jagdesh.

I would also like to thank my friends in life, Vinay Vashishtha, Xiaoning Jin, Naijia Wang, Qian Xu, Yijia Zhang, Sai Zhang, Yipeng Lu, Yu Ye, Zhongwang Liu, Yibo Zhao, Shang Cheng, Yingwei Li, Yi Zhang and Michelle Young.

I would also like to thank my advisors and professors in Shanghai Jiaotong University, Drs Wenyuan Chen, Yubin Miao, Guanglin Shi, Duping Yuan, and Weiguo Pan.

TABLE OF CONTENTS

Page

LIST OF FIGURES

Figure Page

Figure Page

Figure Page

CHAPTER 1

INTRODUCTION

Monitoring vital physiological signals, such as heart rate and breathing pattern, are basic requirements in the diagnosis and management of various diseases [1, 2]. Traditionally, these signals are measured only in hospital and clinical settings. An important recent trend is the development of portable devices for tracking the vital physiological signals non-invasively based on optical methods. These portable devices, when combined with cell phones, tablets or other mobile devices, provide a new opportunity for everyone to monitor one's vital signs anytime and anywhere [3-5].

This thesis describes new methods for non-contact monitoring of several physiological signals in real-time. Signal amplification and minimization of noise due to unwanted body movement forms an important part of the discussion. Based on PPG, I obtained heart rate, pulse transit time (PTT) and blood oxygen saturation at peripheral capillary (SpO_2). Based on tracking body movement, I obtained respiratory signal and ballistocardiogram (BCG). Based on two cardiac signals, I tracked the pulse transit time. Presented methods have been validated by comparison against reference technologies used to measure the corresponding physiological signals. Small scale pilot studies were also conducted to evaluate the reproducibility of the presented work. To demonstrate the robustness of my methods, these studies were conducted on subjects of different age, gender, and skin color.

The presented work contains first demonstrations of non-contact optical imaging methods to determine PTT difference, exhalation flow rate, and BCG. Since the method

presented in this work does not require contact with the subject's body or any extra devices to measure these physiological signals, it has the advantage of providing an easier and burden-free way to measure these parameters when compared to the currently available methods which, to the best of the authors' knowledge, are mainly contact-based, for different measurements.

The novelty of this research includes:

1) The first demonstration of a non-contact method to obtain pulse transit time difference between two photoplethysmogram (PPG) waveforms.

2) The first demonstration of respiratory exhalation flow rate estimation using a video-based method.

3) The first demonstration of blood oxygen saturation level monitoring using a camera system with dual-wavelength illumination.

4) The first demonstration of monitoring ballistocardiogram (BCG)—an important cardiac waveform—without wearing any extra equipment or marker by the subject. The developed method is very robust and easy to implement. Based on the time difference between BCG and PPG, a correlation can be found between the time difference and blood pressure (BP).

I hope that the presented work will help in the development of a new generation of low-cost, non-contact, and convenient monitoring systems that rely on a single primary sensor—a camera—which, by the virtue of its ubiquity, has the potential to enable readily accessible vital physiological signal monitoring. Such monitoring systems have

applications that range from a common household to areas where traditional monitoring systems may be difficult to acquire.

CHAPTER 2

NON-CONTACT PHOTOPLETHYSMOGRAM MONITORING

2.1 Photoplethysmogram Basic Concept and Physiological Relevance

Photoplethysmogram (PPG) tracks the pulsatile blood volume change caused by cardiac activity. It provides valuable information about the cardiovascular system. Portable medical devices have been developed to track physiological signals non-invasively based on monitoring PPG. These PPG-based efforts can be divided into two approaches:

The first one involves contact-based method, whereby a person presses their finger against optical sensors (photodiode or camera) built in the mobile devices for PPG measurement [6]. For devices that use photodiodes, LED-based light sources are used. The amount of light that remains after transmission through or reflection from the fingers, is detected by the photodiode. For camera-based devices, ambient light, or that from the photoflash, may be used. The amount of light that is reflected by the finger is detected by the camera. While useful, this traditional approach requires steady physical contact of one's finger with the PPG devices [7, 8] or the cameras, which makes it impractical for continuous PPG monitoring under normal life conditions, whereby obtaining the measurements requires no special attention or action from user and there is no inconvenience caused by any extra physical burden. Another PPG acquisition approach is based on non-contact mode [9]. For example, heart and breathing rates were obtained from the images of faces [10, 11], upper arms [12] and palms [13] recorded with digital cameras, including industrial cameras [14-16], smartphone cameras [17] and webcams [18, 19].

PPG measured at a single wavelength of light can be used to monitor heart rate, heart rate variability (HRV) and respiration rate [10, 20, 21]. PPGs measured at two different wavelengths of light can be used to measure blood oxygen saturation [14, 16, 22]. Two PPGs, or one PPG with another cardiac signal, like electrocardiogram (ECG) or BCG, can further provide PTT [14, 23, 24].

Non-contact PPG measurement by using camera has been demonstrated by many researchers. Despite of the attractive features of imaging-based non-contact approach, the signals extracted from the images contain noise from various sources [25]. To combat the noise issue, Poh et al. [18, 19] used an independent component analysis (ICA) method that separates a multivariate signal into additive subcomponents supposing the mutual statistical independence of the non-Gaussian source signals. Using ICA, they demonstrated the detection of heart rate, which typically varies between 0.8 - 3 Hz. Verkruysse et al. [10] determined a movement artifact map by averaging the powers at bandwidths around the heart rate. These efforts helped to minimize unwanted noise in the measured heart rate signals.

PTT is an artifact of PPG, and is related to blood pressure pulse wave velocity (PWV), which can indicate cardiovascular parameters, such as arterial elasticity and stiffness [26, 27]. Traditionally, PWV has been measured using a galvanometer [28] and ultrasound techniques [29, 30]. Recently, PTT was determined by performing simultaneous ECG and PPG [31-33]. For example, Babchenko et al. [34] used contact pulse oximetry to determine the difference in PTT of left index finger and left second toe. The PTT difference is related to the change in arterial distensibility due to epidurally induced sympathetic block.

The acquisition of PTT related information has the potential to measure parameters that can help diagnose cardiovascular diseases.

2.2 Method of Measurement

A schematic illustration of the experimental setup for non-contact PPG monitoring is shown in Figure 2-1. Different digital cameras, including Logitech colored webcam (HD 720p), Pike black and white camera (F-032B) and Pike color camera (F-032C), were used to capture videos of each subject's face, palms and upper body. These cameras (colored or black and white) have different inherent noise, but they all produced satisfactory results in terms of determining the physiological parameters. The videos were taken indoors under ambient light condition, using 60 W fluorescent lamps at a height of 5 m for illumination. More controlled light sources, including LEDs and desk lamps, were also used, but no evident improvement in the signals was detected as they all provided sufficient illumination. The subjects were asked to sit at a distance of approximately 50 cm from the camera lens. As long as good quality and clear focus were guaranteed for the image, distance between the camera and the subject did not affect the signals within a range of 30 cm to 80 cm. All the videos and data were analyzed with a Matlab based user interface. The user interface was designed to show the real-time video of the user, allow the selection of regions of interest (ROI), perform signal processing of the data in the ROIs to determine the physiological signals, and display the results in real-time.

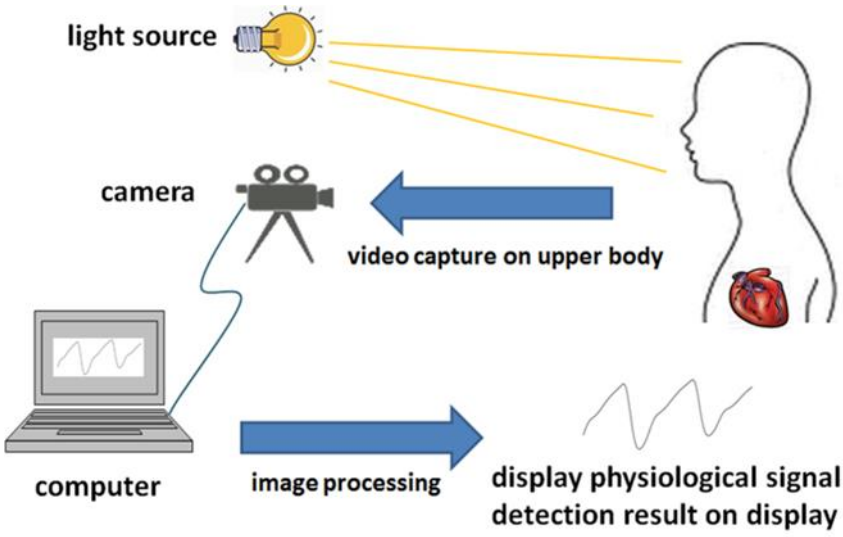

Figure 2-1 Schematic Illustration of Experimental Setup.

For heartbeat monitoring, a video of a subject's face was recorded for typically ~30 seconds in each experiment and fast Fourier transform (FFT) was performed on the intensity signal averaged over all the pixels in each selected ROI to obtain the frequency spectrum of the detected physiological signal. Note that longer recording times may produce better results, but make the process less user-friendly due to longer testing duration required.

2.3 Obtained Signal and Reference Validation

Using the methods described above, the ROI FFT spectrum of the ROI revealed the heartbeat signal as a peak at a frequency corresponding to the heart rate. In order to optimize the signal-to-noise ratio (SNR), the results of red, green and blue channels were compared, and the green channel was found to give the largest peak amplitude in the FFT spectrum, which corresponds to the strongest heartbeat signal (Figure 2-2 (a)). This finding is supported by previous report [10]. One of the possible reasons is that oxygenated hemoglobin has different light absorption characteristics and it absorbs green light more

than red light. Another possible reason is that green light penetrates deeper into the skin tissues compared to blue light—the former can penetrate epidermis, dermis, and hypodermis layers, while the latter can only penetrate epidermis and dermis layers. Since the SNR may also depend on the selection of ROI, the peak amplitude in each pixel was extracted and plotted on a colormap to analyze the heartbeat signal variation in different facial regions (Figure 2-2 (b)). The regions around lips and nose have larger heartbeat amplitudes, which is consistent with the fact that these regions have more blood vessels. Note that eye regions and face edges also appear to have large heartbeat amplitudes, which are due to body movement, rather than the real heartbeat signals. This conclusion is supported by the SNR colormap, obtained by normalizing the peak amplitude of each pixel in the FFT spectrum with the noise level near the peak (1). The noise is defined as the average power of the noise spectrum around the heart rate peak. The SNR is given as follows:

$$SNR = \frac{peak\ amplitude\ at\ HR}{noise} \quad (1)$$

The SNR colormap shows that the regions around the eyes and edges of faces have rather low SNR values (Figure 2-2 (c)).

For heart rate measurement validation, a Zephyr device was used. The heart rate was measured in beats per minute (BPM) and the ECG raw data was obtained from output files generated by Zephyr.

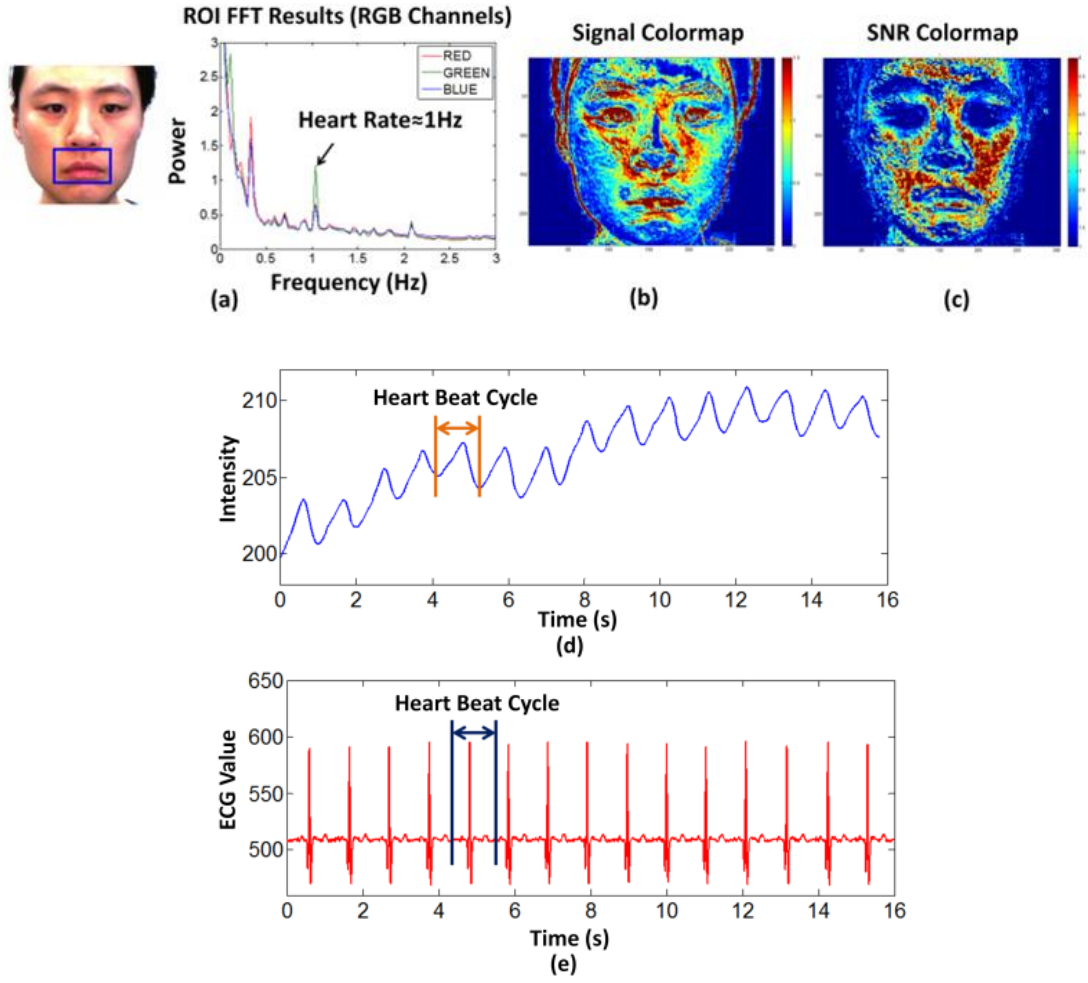

Figure 2-2 PPG Acquisition, Analysis and Validation.
(a) Original image with an ROI (blue rectangle) near the mouth is shown on the left. An FFT spectrum of the ROI is shown on the right. Red, green and blue lines represent the R, G and B color channels respectively, and the green channel gives the strongest heartbeat signal. (b) Colormap of FFT peak amplitude in each pixel at heartbeat frequency (heart rate). The color scale from blue to red indicates the FFT peak amplitude at heart rate. (c) Signal-to-noise ratio (SNR) colormap at heart rate. (d) Heartbeat waveform obtained with the presented method. (e) Heartbeat detection validation. Heartbeat waveform obtained with a commercial device (Zephyr).

2.4 Pulse Transit Time Difference from Two PPGs

Non-contact optical imaging method was also used to determine PTT related information. The variations in PTT to different body parts were obtained by analyzing the time difference of PPG signals measured simultaneously for these parts. The PTT

difference can be obtained from the time difference between the peaks of two PPG signals in the same heartbeat cycle. Figure 2-3 is a representative plot that depicts the method to calculate PTT difference.

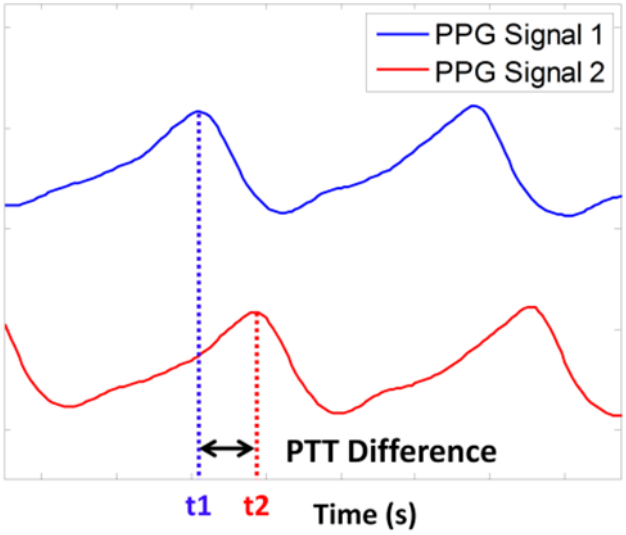

Figure 2-3 PTT Difference Obtained from Two PPG Signals.

The PTT difference in Figure 2-3 can be calculated as

$$PTT\ Difference = t_2 - t_1 . \quad (2)$$

PTT delays were detected between different body parts. In Figure 2-4 (a), the PTT from heart to mouth, and to left and right palms are indicated by t_1, t_2 and t_3, respectively. The ROI selections of three parts from the video sample are shown in Figure 2-4 (b) as three rectangles with different colors. Figure 2-4 (c) shows the PPG signals obtained from the ROIs. Time delays were found between PPG signals from different body parts in every heart cycle. The PPG signal detected from the mouth area (blue curve) arrived earlier than the PPG signals detected from the two palm areas (red and green curves). A delay sample of the delay is shown in Figure 2-4 (c) to illustrate PTT difference between mouth and

palm. PTT difference was not obvious between left and right palms, which is consistent with the observation by Jago et al. [31] with a contact method.

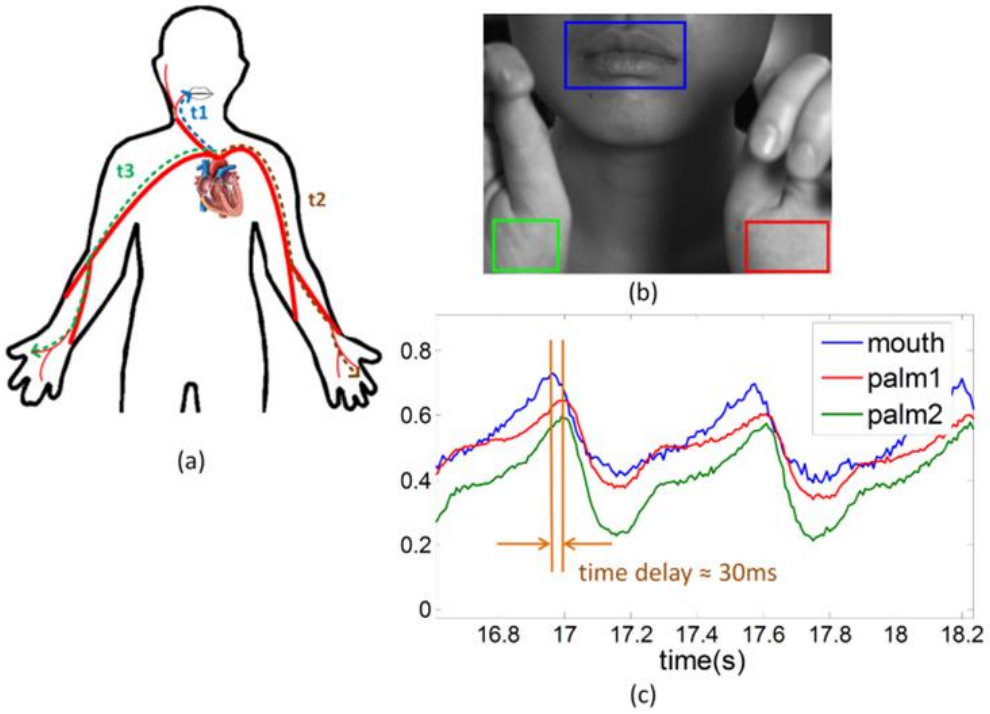

Figure 2-4 PTT Difference among Different Body Parts.
(a) PTT definition for three parts of the body. (b) Corresponding ROIs of three parts. (c) PPG signals obtained from the ROIs. Time delay was about 30ms between PPG signals obtained from mouth and palm.

Several signal processing algorithms were evaluated to determine the PTT difference among different body parts. The first algorithm was based on comparing peak locations of different PPG signals by linear curve fitting method [Figure 2-5]. Matlab function "polyfit" was used to predict a linear curve from the observed signal,

$$p(t) = p_1 t + p_2 . \quad (3)$$

In (3), p_1 and p_2 are the coefficients of the one-degree polynomial $p(t)$ that fits to the detected PPG signal.

Figure 2-5 (a) is an original PPG signal sample obtained from one subject. One heartbeat cycle (indicated by red dashed rectangle) was selected for further analysis. The peak location of the selected signal was estimated by fitting two linear curves on the rising (left part) and falling edge (right part) of the signal (Figure 2-5 (b)). The point of intersection (indicated by the green arrow) of two linear curves is the estimated peak location. PTT differences were determined by comparing the peak locations of PPG signals obtained at different body parts (e.g., mouth and palm).

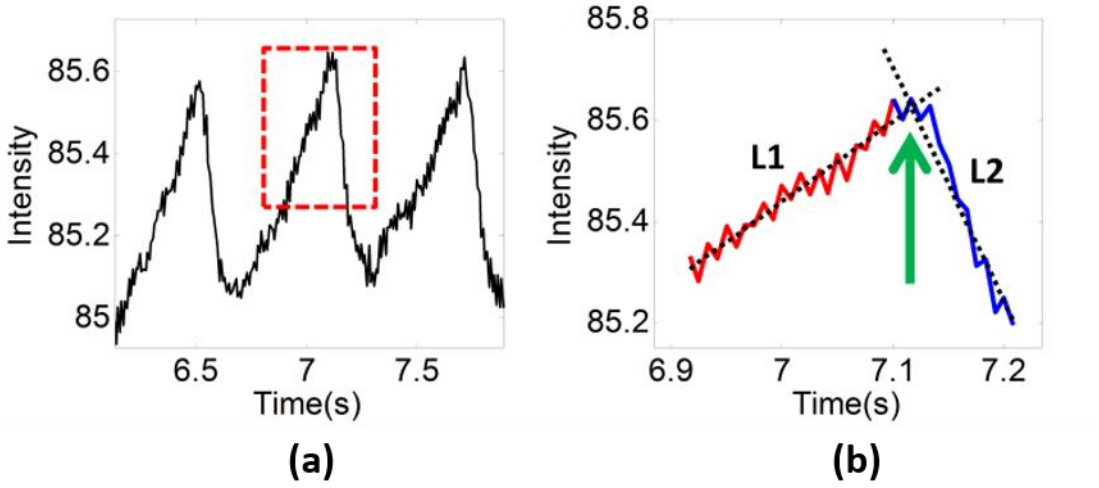

Figure 2-5 Estimate Peak Location by Using Linear Curve Fitting Method.
Take one cycle from PPG signal (a) and use two linear curves (black dashed lines) to fit the original signal from the left part (red) and the right part (blue) independently (b). The point of intersection of two linear curves (green arrow) is the estimated peak location in that particular heartbeat cycle.

Nine tests conducted on one subject were analyzed to obtain the average value of PTT difference between mouth and palm areas (Table 2-1). PTT difference for each test was an average result from all the available heartbeat cycles in that time period. Each test lasted for 30 seconds.

Table 2-1
PPG Delay Estimation Results between Different Sites.
The values are calculated based on linear curve fitting method. The estimated delay values obtained from facial area to two palm areas are similar, about 30-31 ms.

Test No.	Heart Rate (bpm)	PTT Difference	
		from mouth to left palm (ms)	from mouth to right palm (ms)
1	72	22.50	22.28
2	78	34.50	32.37
3	78	28.36	29.35
4	72	30.39	32.23
5	72	23.35	27.82
6	71	33.97	35.64
7	106	25.99	28.26
8	96	34.56	36.04
9	96	34.13	35.61
Average		29.75	31.07
SD/Average		16%	15%

Matlab functions “findpeaks” and “xcorr” were also used to estimate the PTT difference value. Function “findpeaks” provides the peak location of the input data by searching for the local maximum value of the sequence. Function “xcorr” realizes phase shift estimation between two signals by taking their convolution and searching for the delay that gives the largest convoluted result. However, the standard deviations of the calculated PTT differences obtained from these two methods were higher than the standard deviation obtained from the first one (linear curve fitting method). Therefore, the first method was used to estimate the PTT differences among different body parts. Test results in Table 2-1 show that the PTT difference between palm and mouth is about 30 ms. The results are consistent with the values of PTT difference reported by other researchers [28-30]. The accuracy of PTT difference calculation can be further improved at faster video frame rates (current value is 120 frames per second) that help to provide more accurate PPG peak locations.

A small scale pilot study was conducted for PTT difference calculation. Ten tests were conducted on four subjects. The average PTT difference between mouth and palm areas was about 30-40 ms (Table 2-2).

Table 2-2
PTT difference estimation results for four subjects.
The calculated values were based on linear curve fitting method. The average PTT difference between mouth and palm areas was about 35 ms from mouth to left palm and 37 ms from mouth to right palm.

Subject No.	Gender	PTT Difference	
		from mouth to left palm (ms)	from mouth to right palm (ms)
1	female	29.75	31.07
2	female	35.02	32.06
3	male	32.96	41.67
4	male	42.03	43.29
Average		34.94	37.02
SD/Average		15%	17%

2.5 Discussion

Non-contact PPG monitoring can be affected by motion artifacts. Using motion tracking based on phase correlation may help to correct some of the unwanted motions (more details in Section 4.1). Other methods may also help to improve the influence of body motions, such as, using the combination of multiple color channels with different weighing factors, instead of using a single channel [20].

The PTT difference obtained from two PPGs is potentially correlated with blood pressure. The accuracy of PTT difference is limited by video temporal resolution. To see an obvious PTT difference during blood pressure change, it is preferable to measure the two corresponding PPGs at locations which are not close to each other. For example, PTT difference between head and foot will be more obvious than that between head and neck. However, using a single camera to capture video including two body parts with enough

distance is not very practical for implementation. Based on this concern, measuring the PTT difference from two cardiac signals at the same location will be a potential solution, which will be discussed in more detail in Section 6.

CHAPTER 3

NON-CONTACT BLOOD OXYGEN SATURATION MONITORING

3.1 Physiological Relevance and Related Work

Oxygen saturation is a vital physiological parameter. It is a relative measure of the oxygen amount dissolved or carried in a given medium, such as blood. It indicates whether a person has sufficient supply of oxygen and reflects the health level of the cardiorespiratory system. Continuous monitoring of oxygen saturation level is important in detecting hypoxemia under many medical situations, including anesthesia administration, sleep apnea, and parturition. It is employed in intensive care, operating room, emergency care, neonatal care, sleep study, and veterinary care [35].

Mixed venous oxygen saturation (SvO_2), tissue oxygen saturation (StO_2) and arterial oxygen saturation (SaO_2) are a few major methods used for the determination of oxygen saturation levels in human body. SvO_2 measures the oxygen remaining in the blood after passing through the capillary bed, which is an indicator of moment-to-moment variation between oxygen supply and demand [36]. Fiber optics catheters are used when monitoring SvO_2. StO_2 provides an assessment of tissue perfusion and it can be measured by near infrared spectroscopy. SaO_2 measures oxygen saturation in the arteries. An estimation of SaO_2 at peripheral capillary is called SpO_2, which is the primary focus of this chapter. Unlike traditional SaO_2 measurement, which is normally conducted invasively via a blood test with a blood gas analyzer, SpO_2 can be measured by noninvasive methods. Monitoring SpO_2 provides a quick and convenient assessment of a person's oxygenation status. The most widely used device for SpO_2 monitoring is pulse oximetry, which is often

attached to the finger for measurement purpose. The hardware implementation of pulse oximetry includes two main components: 1) an illumination source usually composed of a dual-wavelength LED, and 2) a photodetector—typically a photodiode. SpO_2 values typically range from 95% to 100% in healthy individuals. Continuous low SpO_2 levels (< 90%) may indicate an oxygen delivery problem [37].

Recent technological advances have enabled measurements of some of the physiological signals using non-contact methods [10, 14, 19]. Remote SpO_2 detection provides people with a method to measure oxygen saturation non-invasively under normal daily setting. Absence of physical contact between the subject and the device allows for a more comfortable and less stressful measurement condition. The inaccurate SpO_2 readings caused by varied pressure applied from finger to the contact sensor can also be avoided [38], besides preventing skin irritation that can occur in some individuals, especially infants, during extended monitoring periods. Non-contact pulse oximetry also provides a suitable SpO_2 measurement alternative for individuals with finger injuries, or for those with poor peripheral perfusion or dark pigmentation on fingers, for whom traditional pulse oximetry may otherwise lead to inaccurate measurements [39].

In recent years, researchers have attempted different SpO_2 measurement approaches using non-contact methods. Humphreys et al. [40, 41] used a CMOS camera with LED arrays that emit two different wavelengths as the light source for non-contact pulse oximetry. Due to low frame rate and sensitivity to ambient light, the noise in the measured PPG signals was too large to obtain accurate SpO_2 values. Wieringa et al. [16] also used a CMOS camera, but with three different wavelengths to investigate the

feasibility of an "SpO_2 camera". However, no SpO_2 results were presented due to poor SNR of the PPG signals. Kong et al. [42] used two CCD cameras, each mounted with a narrow band-pass filter to capture PPG signals at two different wavelengths (520 nm and 660 nm) in ambient lighting condition. The test only covered a narrow SpO_2 range (97%-99%). For practical applications, such as clinical settings, it is necessary to be able to measure SpO_2 over a wider range (at least 80%-100%). Tarassenko et al. [43] and Ufuk et al. [44] used a camera to calculate SpO_2 based on the PPG information obtained from the RGB channels under ambient lighting condition. Other researchers have found that the PPG signals extracted from the red and blue channels were noisier than those extracted from the green channel [10, 45, 46]. Moreover, for digital cameras, each color channel (red, green, or blue) covers a band of optical spectrum [47] with a width of ~100 nm, which is different from the traditional pulse oximetry method that uses monochromatic light sources with wavelengths selected to maximize the detection sensitivity of oxygenated and deoxygenated hemoglobin in blood. Tsai et al. [48, 49] used a CCD camera with red and infrared LEDs to take still images of hand, and analyzed SpO_2 by looking into the reflective intensity of the shallow skin tissue. These authors compared the SpO_2 results against partial pressure of oxygen values (PaO_2), instead of the standard pulse oximetry. Although they showed correlation between the results obtained using the two methods, a direct demonstration of SpO_2 measurement is still lacking.

3.2 SpO_2 Measurement Using a Dual-Wavelength Imaging System

SpO_2 is the percentage of oxygenated hemoglobin at peripheral capillary and can be expressed by the following equation,

$$SpO_2 = \frac{[HbO_2]}{[HbO_2]+[Hb]} \times 100\%. \quad (4)$$

where $[HbO_2]$ is the concentration of oxygenated hemoglobin and [Hb] is the concentration of deoxygenated hemoglobin.

Traditional pulse oximetry measures SpO_2 based on the differential absorption of light by HbO_2 and Hb at two wavelengths. Depending upon the optical absorption spectrum of HbO_2 and Hb shown in Figure 3-1, it is possible to select two wavelengths, λ_1 and λ_2, such that absorbance by HbO_2 is more at λ_2 than at λ_1, while the absorbance by Hb is more at λ_1 than at λ_2.

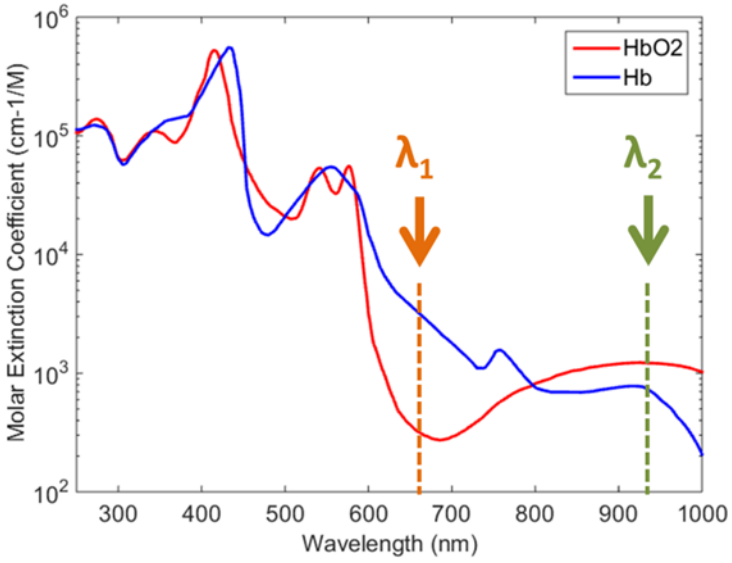

Figure 3-1 Absorption Spectrum of HbO_2 and Hb.
The extinction coefficients are used from [50] with permission.

The Beer-Lambert law—widely used to determine a solution's concentration by optical transmittance measurement—states that light absorption by a substance in a solution is proportional to its concentration [51]. Pulse oximetry assumes that the pulsatile component (AC) of optical absorption originates from the pulsatile arterial blood, and the non-pulsatile component (DC) contains contributions from non-pulsatile arterial blood, venous blood, and other tissues. The pulsatile signals (AC) can be normalized by the non-pulsatile signals (DC) at λ1 and λ2, to give the pulsatile absorbance rates as follows,

$$R_{\lambda_1} = \frac{AC_{\lambda_1}}{DC_{\lambda_1}}. \quad (5)$$

$$R_{\lambda_2} = \frac{AC_{\lambda_2}}{DC_{\lambda_2}}. \quad (6)$$

The ratio of absorbance at two wavelengths is defined as ratio of ratios, RR,

$$RR = \frac{R_{\lambda_1}}{R_{\lambda_2}} = \frac{AC_{\lambda_1} / DC_{\lambda_1}}{AC_{\lambda_2} / DC_{\lambda_2}}. \quad (7)$$

RR can be regarded as nearly linear with respect to SpO_2 [3, 42, 44],

$$SpO_2 = k \times RR + b. \quad (8)$$

where *k* and *b* are linear equation coefficients. Thus, SpO_2 value can be obtained by measuring RR. This dual-wavelength ratio method provides an easy way to determine SpO_2, and the result is independent of both light path length and concentration of blood constituents that absorb light.

The presented SpO_2 detection method is based on the same optical principles as the traditional pulse oximetry. A key difference is the ability of the presented work to track

SpO_2 change using a non-contact method based on the reflected light. Further details of this method are provided in Section 3.4.

3.3 Light Source Selection

As mentioned earlier, SpO_2 detection using the RR value requires employing at least two wavelengths. For accurate measurement, it is preferable that: 1) the measured PPG signals have high SNR at both wavelengths, and 2) optical absorption associated with HbO_2 and Hb are opposite and the differences are large at the two wavelengths, as shown in Figure 3-1.

The traditional contact-based pulse oximetry uses a dual-wavelength LED at red (λ = 660 nm) and near infrared (NIR, λ = 940 nm) wavelengths as light source, and a photodiode as light detector. For transmission mode pulse oximetry, the LED and photodiode are placed at either sides of the tissue (e.g., finger or earlobe), and for reflection mode pulse oximetry, the LED and photodiode are positioned on the same side of the tissue. As per Figure 3-1, the red light at 660 nm is absorbed more by Hb than by HbO_2, while the NIR light at 940 nm is absorbed more by HbO_2 than by Hb. The 660 nm and 940 nm wavelength combination produces high quality data for the contact pulse oximetry, but it is not suitable for the presented non-contact method.

It was observed that the use of red LED at 660 nm for the non-contact method results in poor PPG signal. To find a suitable replacement for the 660 nm LED, the non-contact PPG signals were evaluated at various wavelengths, ranging from 470 nm to 940 nm. It is observed that the best PPG signal is obtained when green light is used, which is consistent with the literature [10, 45, 46]. However, the optical absorption difference

between HbO_2 and Hb at green is small (Figure 3-1), thereby making green unsuitable for SpO_2 measurement. Blue was ruled out because its optical absorption is similar to NIR with high HbO_2 absorbance and low Hb absorbance despite the fact that its use produces good quality PPG signal [52]. Orange (λ = 590 nm to 635 nm) was determined to be the most suitable substitute to red for this application because its optical absorption property fulfils the specified criteria—high Hb and low HbO_2 absorbance—and due to the superior PPG signals (shown in Figure 3-2) measured via the non-contact method when using orange (λ = 611 nm) LED, as compared to red (λ = 660 nm) LED.

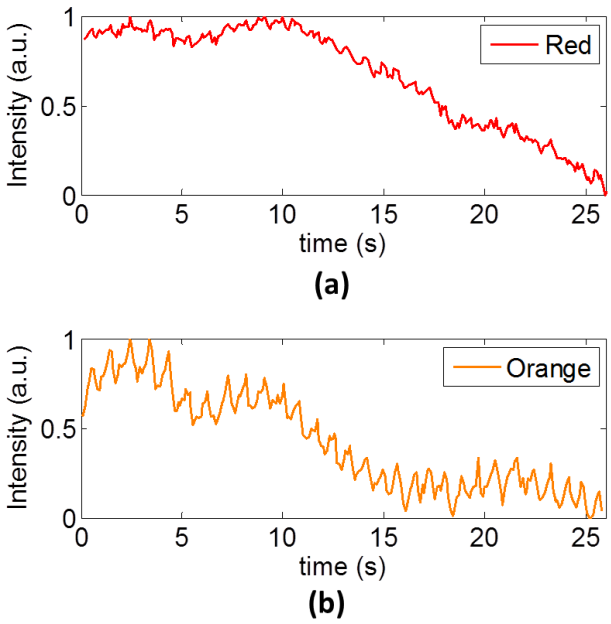

Figure 3-2 PPGs Measured Simultaneously with Red and Orange LEDs.

I also examined the suitability of the 940 nm LED—used in conventional contact pulse oximetry—for the presented imaging system, and found the PPG signal obtained using it to be unsatisfactory due to low SNR. The primary reason for this was the low quantum efficiency of the CMOS imager at 940 nm. NIR at wavelength 880 nm was found

to provide better quality PPG signal obtained using the camera sensor. Moreover, 880 nm and 940 nm have similar optical absorptions by HbO_2 and Hb. These two reasons prompted the use of 880 nm LED, instead of 940 nm LED, in conjunction with the 610 nm orange LED for the presented method.

Performance of the 610 nm orange and 880 nm NIR combination was examined with a simulation of the dependence of RR on SpO_2 from 70% to 100%. The simulation was based on the Beer-Lambert law and the assumption that absorption of light in blood is only related to HbO_2 and Hb, which lead to the following RR equation,

$$RR = \frac{s \times \varepsilon_{HbO_2\_\lambda_1} + (1-s) \times \varepsilon_{Hb\_\lambda_1}}{s \times \varepsilon_{HbO_2\_\lambda_2} + (1-s) \times \varepsilon_{Hb\_\lambda_2}}. \quad (9)$$

where *s* is the oxygen saturation (SpO_2), and are the extinction coefficients of HbO_2 and Hb at the two wavelengths [51]. The simulation result, as shown in Figure 3-3, indicates that SpO_2 is linearly proportional to RR ($R^2 \sim 1$) with a maximum error < 0.6% over a broad range (70%-100%), and can be approximated by (8). The linear relationship is consistent with other studies [3, 42, 44]. Coefficient k, in (8) can be estimated from the linear fit curve slope, which is −12.1 as shown in Figure 3-3.

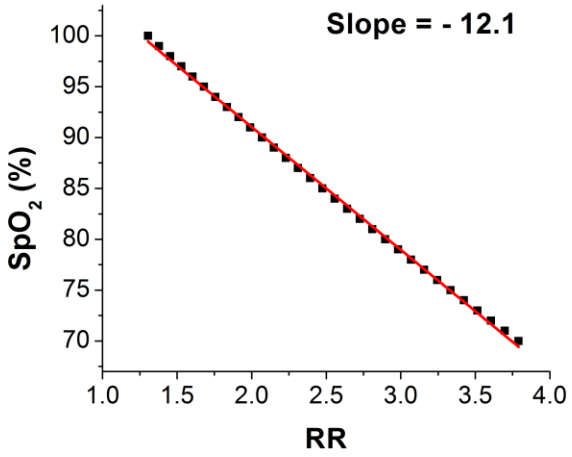

Figure 3-3 Relationship between SpO2 and RR (with wavelengths at 610 nm and 880 nm) based on (6) using extinction coefficients from [45]. The red line is a linear fit.

Similar simulations with different wavelength combinations were carried out to determine the best wavelength combination for accurate SpO_2 measurement (see Figure 3-4). For easy comparison of results at different wavelength combinations, each plot was normalized by the corresponding RR value at 100% SpO_2. The steeper the curve, the more sensitive a combination is to SpO_2 change. The red/NIR combination, which is widely used in the traditional pulse oximetry, shows the steepest curve. When SpO_2 drops from 100% to 70%, RR changes by 319%, indicating that this combination is most sensitive to SpO_2 change. However, for the green/NIR and blue/NIR combinations, RR changes by only 14% and 5%, respectively, indicating their unsuitability to detect SpO_2 changes. The orange/NIR combination shows a change of RR by 190%. Although it is not as good as the red/NIR combination, it is the best choice for non-contact SpO_2 tracking when the SNR of the PPG signals are considered.

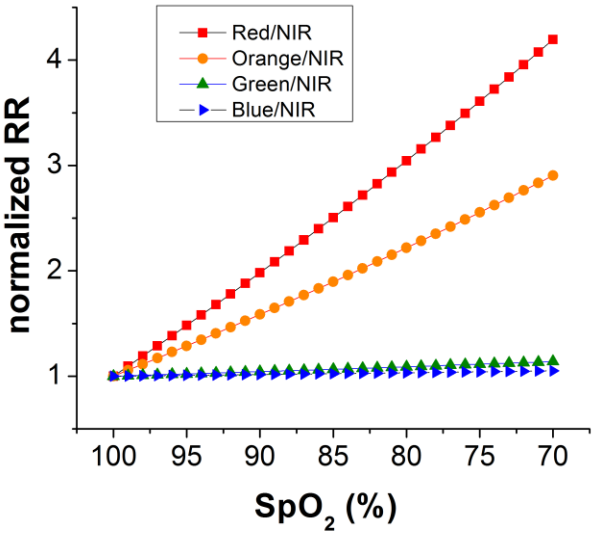

Figure 3-4 Simulated Plots of Normalized RR vs. SpO_2.
Based on four different wavelength combinations. (1) Red (λ = 660 nm) and NIR (λ = 880 nm); (2) Orange (λ = 610 nm) and NIR (λ = 880 nm); (3) Green (λ = 528 nm) and NIR (λ = 880 nm); (4) Blue (λ = 470 nm) and NIR (λ = 880 nm). The extinction coefficients used are from [50].

3.4 Hardware Implementation

The experimental setup is shown in Figure 3-5. A PixeLINK monochromatic camera PL-B741EU with a Fujinon HF16HA-1B 16 mm f/1.4 fixed focal lens was used to record the videos. The illumination system consisted of two identical LED arrays placed symmetrically on the left and right sides of the camera. Each array included alternating rows of NIR (QED223, Fairchild Semiconductor) and orange (SLI-570DT3F, Rohm Semiconductor) LEDs. A microcontroller (Texas Instruments MSP430F5348) was used to generate LED and camera trigger signals to switch the NIR and orange LEDs on and off alternatively, so as to capture an image every 50 ms at the camera's trigger signal rising edge when either the NIR or the orange LEDs were on. The camera was triggered 20

times/s, so for each wavelength, the corresponding frame rate was 10 frames/s. All videos were taken indoors without ambient lights to avoid noise.

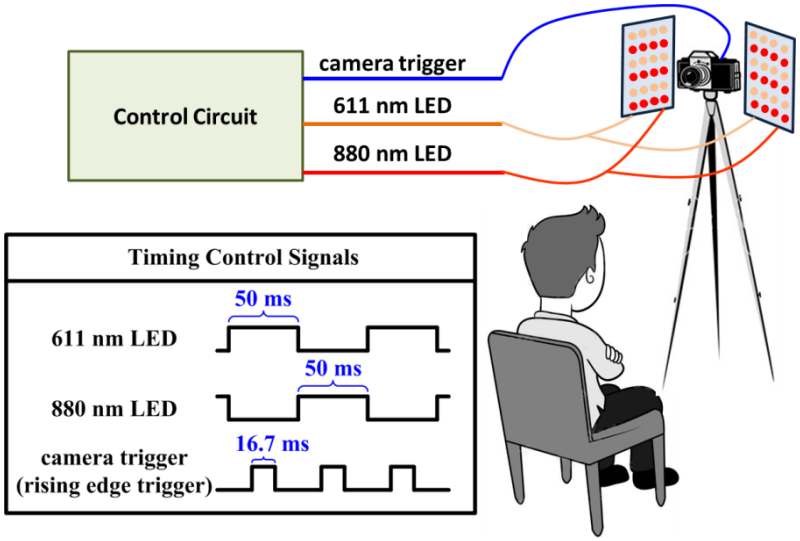

Figure 3-5 Experimental Setup and Control Signals.

3.5 Design of Experiment

The subjects were asked to sit still approximately 30 cm from the camera and LED arrays. As long as clear focus and proper size were guaranteed for the region of interest (ROI), the distance did not affect the signal much, which was partially due to AC/DC normalization. A blindfold was used for comfort and eye protection. Each experiment lasted 5 minutes. As mentioned earlier, the normal SpO_2 range is 95-100% in healthy people. To validate the presented method for low SpO_2 (<90%), the subjects were asked to hold their breath until they felt uncomfortable. This resulted in their blood reaching a low oxygen saturation level—a technique also used by other researchers [3, 42]. There is no known risk associated with holding breath for 0.5-1.5 minutes in healthy people. To produce a noticeable drop in SpO_2, the subjects must hold their breath for at least 30 seconds. Notwithstanding this equal time duration, the SpO_2 drop observed varied from

one individual to another because of the varying lung capacity and hemoglobin oxygenation efficiency. It was also noticed that after holding breath for one minute, SpO_2 dropped below 90% in some subjects while in others, the drop was much smaller.

The subjects were asked to breathe normally for the first two minutes, during which the SpO_2 value was stable due to the sufficient oxygen supply. After this initial two-minute period, each subject was asked to hold breath as long as possible to produce an SpO_2 drop. When the subject resumed breathing, SpO_2 recovered to the same level as that before holding breath, usually within a few seconds.

SpO_2 measurements were also carried out simultaneously using a commercial contact pulse oximeter (Homedics PX-100) for comparison. The commercial device provided a reading nearly every 10 seconds.

3.6 Data Processing

Previous study [14] has shown that the area around the lips provides a suitable region for good PPG signal measurement. For this reason, an area of 160 × 120 pixels around the lip was selected as the ROI. After capturing the videos, the ROI was analyzed using the following procedure. The acquired images were sorted into two groups, viz. NIR and orange as shown in Figure 3-6, based on the wavelength at which they were captured.

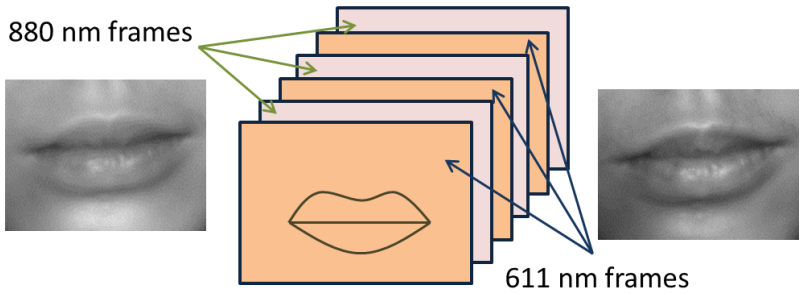

Figure 3-6 Image Sequence Acquisition with Two Different Wavelengths.

In each group, the image intensity was averaged over all the ROI pixels in every frame to obtain the PPG signal at the corresponding wavelength. Each of the two PPG signals was divided equally into ten second subsets to provide SpO_2 data with a time resolution similar to the commercial contact pulse oximeter. For each of these subsets, the AC and the DC components of the PPG signal were obtained using the average peak-to-peak (see Figure 3-7) and average value, respectively. Fast Fourier transformation (FFT) can also be used to extract the PPG signal AC component [53-58], but it works well only when the heart rate remains constant, and yields inaccurate results when heart rate variability is high. The RR values were determined from (4) by using the measured AC and the DC PPG signal components. To extract SpO_2 from RR, equation (5) was used, where k was determined from the slope of the plot shown in Figure 3-3, and the intercept b was determined from the baseline SpO_2 level and corresponding average RR value obtained during the initial two minutes of each test.

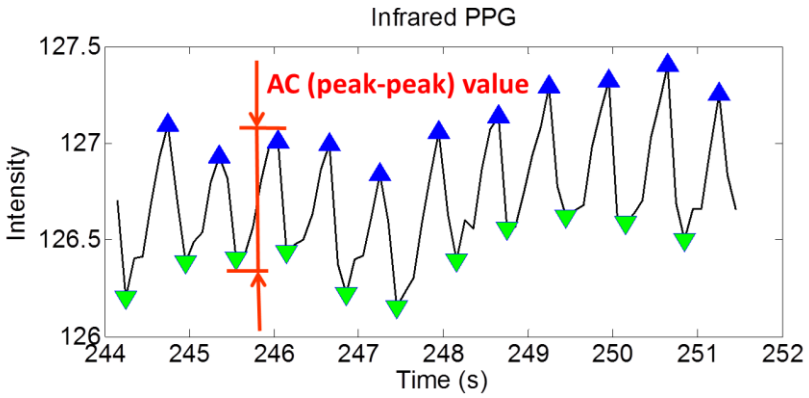

Figure 3-7 AC Value Obtained from PPG.

3.7 Validation of Wavelength Selection

I first validated the detection of non-contact PPG signals at 611 nm and 880 nm. I recorded PPG signals at the two wavelengths simultaneously, both showing heart beating clearly as plotted in Figure 3-8. AC/DC normalization was used for compensating the difference in image intensities at the two wavelengths (2, 3). FFT spectra of the simultaneously recorded PPGs at the two wavelengths show pronounced peaks at 1.5 Hz, which correspond to the heart rate.

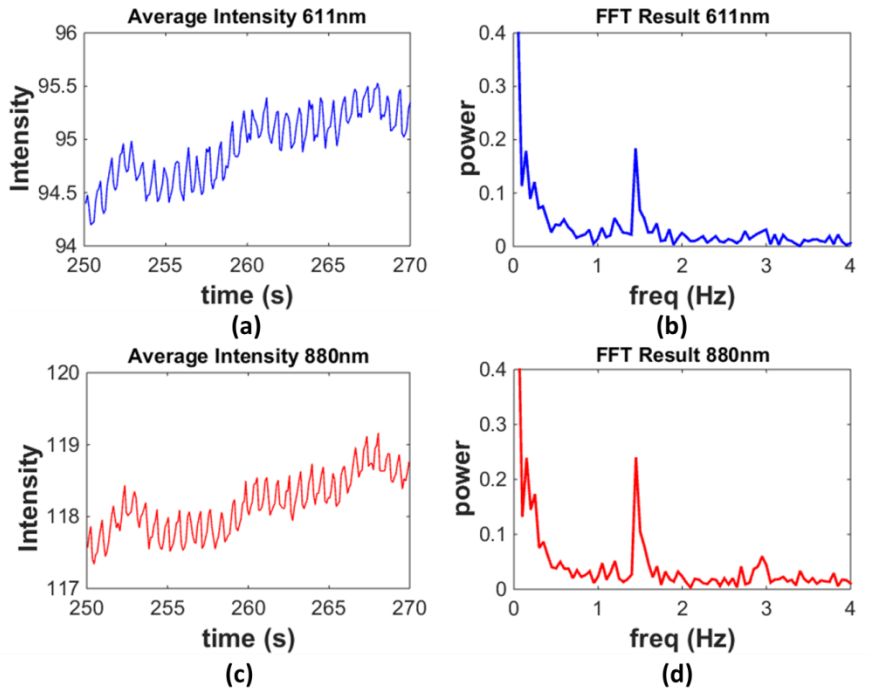

Figure 3-8 PPGs at Two Wavelengths.
Signals obtained at 611 nm and 880 nm (a, c), and the corresponding FFT spectra (b, d).

When SpO_2 drops, HbO_2 concentration decreases, and Hb concentration increases. In this case, it is expected that more orange light and less NIR light will be absorbed. Consequently, the reflectance of orange light will drop and that of the NIR light will increase. When SpO_2 increases, opposite changes in the reflectance are expected. Figure 3-9 shows that the average intensity at 880 nm increased when the subject held breath (SpO_2 dropped) and decreased after the subject resumed breathing (SpO_2 increased). It also shows an opposite trend at 611 nm. These observations are consistent with the optical absorption properties of HbO_2 and Hb at 611 nm and 880 nm.

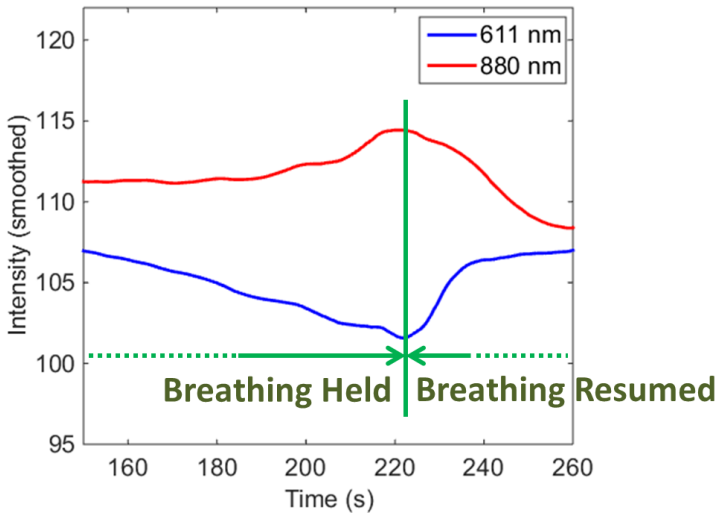

Figure 3-9 Image Intensity Changes Due to SpO_2 Variation.
Each PPG signal has been smoothed by a 100-point moving average filter.

3.8 SpO_2 Measurement Results

Figure 3-10 shows two sets of measurements performed for validation purpose, wherein SpO_2 values were obtained using the presented method (black curve) and were compared against those obtained using the reference device (red curve) every ten seconds over a five minute measurement duration. The stable SpO_2 value at 98% corresponds to the normal breathing period of two minutes and the evident reduction corresponds to the time period for which breath is held. The SpO_2 value restoration corresponds to the resumption of normal breathing. A delay (~10 s) in the reading of the reference pulse oximeter was corrected for comparison with the non-contact SpO_2 detection. The comparison shown in Figure 3-10 indicates that the SpO_2 measured using the non-contact method is consistent with that measured using the contact-based reference method.

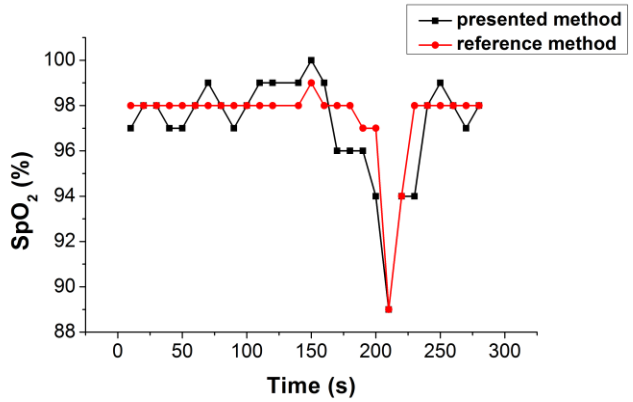

(a)

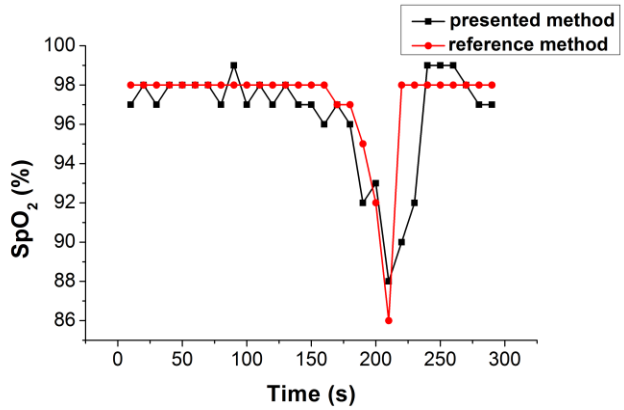

(b)

Figure 3-10 SpO_2 Monitoring with Presented Method and Reference.
(a, b) SpO_2 measured using a pulse oximeter (reference method, red curve) and using the presented method (black curve).

3.9 Small Scale Pilot Study

To demonstrate the robustness of the presented non-contact method to monitor SpO_2, a small-scale pilot study was conducted and statistical analysis of the data was completed. Six subjects were enrolled in the Institutional Review Board (IRB) study approved by Arizona State University (No. STUDY00002240). The subjects were of different genders (three males, three females), ages (27.3 ± 2.8 years old, mean ± SD), and skin colors. Informed consents were obtained from all the subjects following an approved

protocol. None of the subjects had any known respiratory disease. I repeated the test as described in the last section on different subjects and compared the lowest SpO_2 values determined using the presented method and reference pulse oximetry. Figure 3-11 shows a plot of the lowest SpO_2 values from 43 tests and linear least square regression. A good linear correlation ($R^2 = 0.87$) is found between the presented and reference methods over a wide range of oxygen saturation levels. Slope of the linear fitting curve is about 0.86, with standard error of 0.05, which is smaller than the ideal value of 1. The data is dispersed around the linear curve, which may be attributed to subject movement, and light scattering effects. The red line is a linear fit.

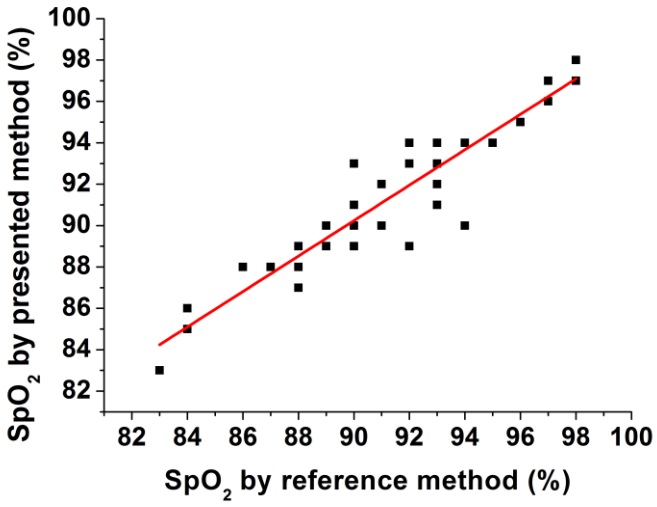

Figure 3-11 Correlation with Reference Method.
Correlation between the lowest SpO_2 values obtained from the presented non-contact and reference contact methods.

Bland–Altman plot was used to further evaluate the test results (Figure 3-12). The mean of the differences between the presented method and reference method is -0.07%. The interval for 95% limits of agreement between the two methods is from -2.65% to 2.51%, which is calculated by mean difference ± 1.96 × standard deviation of the

differences. The root-mean-square error (RMSE) is 1.3 and r is 0.936 ($p < 0.001$). Since $p < 0.05$ indicates a significant correlation between the two methods under comparison, it can be concluded that the observed correlation between the presented non-contact SpO_2 detection method and the traditional contact pulse oximetry is statistically significant.

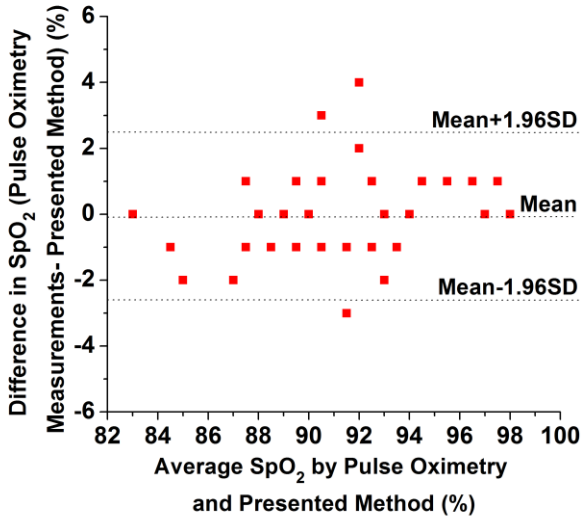

Figure 3-12 A Bland–Altman Plot for Analysis.
The plot shows the difference between the SpO_2 values measured using the presented non-contact method and the commercial contact pulse oximetry vs. the average values of the two methods.

3.10 Discussion

The lowest SpO_2 observed during testing for the presented work was 83%. Lower SpO_2 values were difficult to achieve by holding breath in healthy individuals. A person with SpO_2 lower than 80% is considered to be in a state of hypoxia. The presented method was validated for SpO_2 values ranging from 83%-100%, which is the normal oxygen saturation level range in most healthy individuals. Thus, the presented method can be used for daily SpO_2 monitoring.

Compared to the traditional contact pulse oximetry, non-contact pulse oximetry is considerably more challenging. This work demonstrated the feasibility of measuring SpO_2 accurately with a non-contact method, but there are several improvements that can be made in the future, some of which are discussed here. Firstly, the camera used for PPG signal detection in the presented work has a sampling rate of 20 Hz, which is much lower than the 480 Hz sampling rate that the photodiodes used in the traditional pulse oximeter can typically reach [41]. Yet another related issue is the missing frames, which can range from 5%-10% of the total number of captured frames, due to the camera's hardware and software limitations. Both of these issues can be addressed by using a higher quality imaging system. Secondly, although this work's scope is limited to the validation of the presented non-contact method for SpO_2 tracking with subjects sitting relatively still on a chair, motion tracking algorithms can be used in the future works to mitigate PPG signal deterioration arising from subject movements [59, 60] so as to improve the system's robustness and augment the extent of utilization. Lastly, in the presented work, a commercial pulse oximeter was used as reference instead of arterial blood gas analysis—the gold standard for pulse oximetry development. The error of commercial pulse oximeter is about $\pm$ 2-3% for normal SpO_2 (95%-100%) and can be as large as $\pm$ 8% when SpO_2 drops to very low levels (< 80%) [61]. Replacing commercial pulse oximeter with blood gas analyzer (e.g. CO-oximeter) to perform in vivo calibration will improve the accuracy of the presented method. However, blood gas analysis is typically an invasive technique and requires special equipment usually only available in clinical settings—the lack of which during the development of the presented system limited the analysis to the use of a theoretical model

such as (6), which is derived using the Beer-Lambert law. As stated earlier, the curve for RR and SpO_2 was approximated to be linear over the SpO_2 range of 70% to 100% when using (6) and the linear coefficient *k* was determined for it. Nevertheless, the Beer-Lambert law does not take into account the effects of light scattering at the skin surface when measuring PPG in reflective mode. Light scattering changes the optical path length and thus affects the total apparent absorbance [61]. Building a more accurate optical model to incorporate the effects of light scattering is a difficult task. Therefore, other researchers adopt approaches that include development and application of advanced mathematical models [62, 63] or empirical correction schemes to better describe the relationship between RR and SpO_2. These correction methods could be implemented in the future works to further improve the presented method.

CHAPTER 4

NON-CONTACT RESPIRATION MONITORING

4.1 Method of Measurement

I also used imaging-based method to monitor respiration activity. The breathing pattern was determined by detecting and analyzing the body movement associated with breathing using camera. Different parts of the body move with breathing differently. Chest and abdomen may have the largest movements with breath [64], but these regions are not easily accessible to camera for imaging under normal conditions. For this reason, the face, the neck and upper body are preferred as sites for measuring breathing pattern. A region of 40 x 40 pixels around the edge of shoulder was selected to be the ROI for breathing detection (Figure 4-1, left panel). The ROI size was chosen after considering an optimal size that was large enough to capture the complete range of possible shoulder movement due to breathing activity while at the same time was sufficiently small so that it could still sensitively track small shoulder movements due to breathing. Then the derivative of the ROI was taken along vertical direction to obtain a differential image of the ROI. Shoulder edge in this differential image was revealed as a bright line (Figure 4-1, right panel).

The line location indicates the position of the shoulder edge. To accurately determine the shoulder position, the differential image of the selected ROI was divided into two equal portions along the shoulder edge. The derivative of the ROI of the top portion is referred to as *dA* and that of the bottom portion as *dB*. When the shoulder moves up and down with breathing, *dA* increases (or decreases) and *dB* decreases (or increases). The vertical movement of shoulder can be determined by

$$dI = \frac{dA - dB}{dA + dB}. \quad (10)$$

The difference, $dA - dB$, in (10) is sensitive to the vertical movement and is immune to common noise in dA and dB. Dividing $dA - dB$ by $dA + dB$ further reduces noise associated with the intensity fluctuations of the light source. For example, if the light changes, dA and dB will change in a similar way, and the normalization will remove the effects of light intensity instability. The value dI is calculated for every frame, and plotted against time after applying a low-pass filter with a cut-off frequency of 2 Hz.

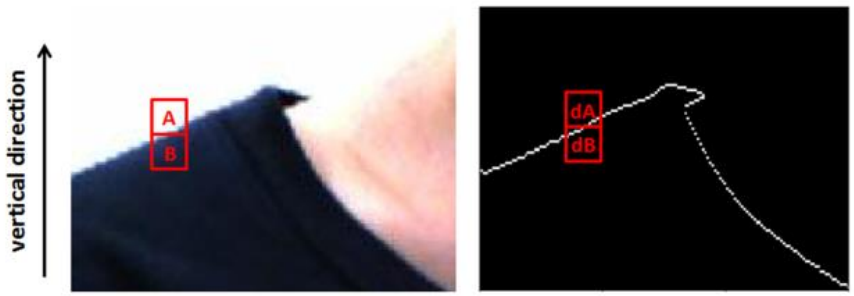

Figure 4-1 Original and Derivative Images.
Left: A zoomed-in image showing subject's right shoulder. Right: Derivative image with respect to vertical direction, where the shoulder edge is shown as a bright line.

The accuracy of breathing pattern measurement may be affected by body movements unrelated to breathing during these measurements. Compared with heart rate monitoring, it is even more challenging to track breathing pattern, especially breath-by-breath, because breathing frequency is much lower than the heart rate. In a typical ambient environment, low frequency noise, particularly noise associated with body movement, is much greater than noise at high frequencies.

I implemented a motion tracking algorithm to correct such motion artifacts based on the phase correlation method [65]. The algorithm checked the shift of the ROIs due to

the body movement approximately every two seconds and corrected it by updating new locations of the ROIs (Figure 4-2). Suppose the original location of one pixel was (x, y), the updated location would be

$$\begin{cases} x_{new} = x + shift\_x \\ y_{new} = y + shift\_y \end{cases}. \quad (11)$$

where *shift_x* and *shift_y* were the location differences along the horizontal and vertical directions calculated by phase correlation method.

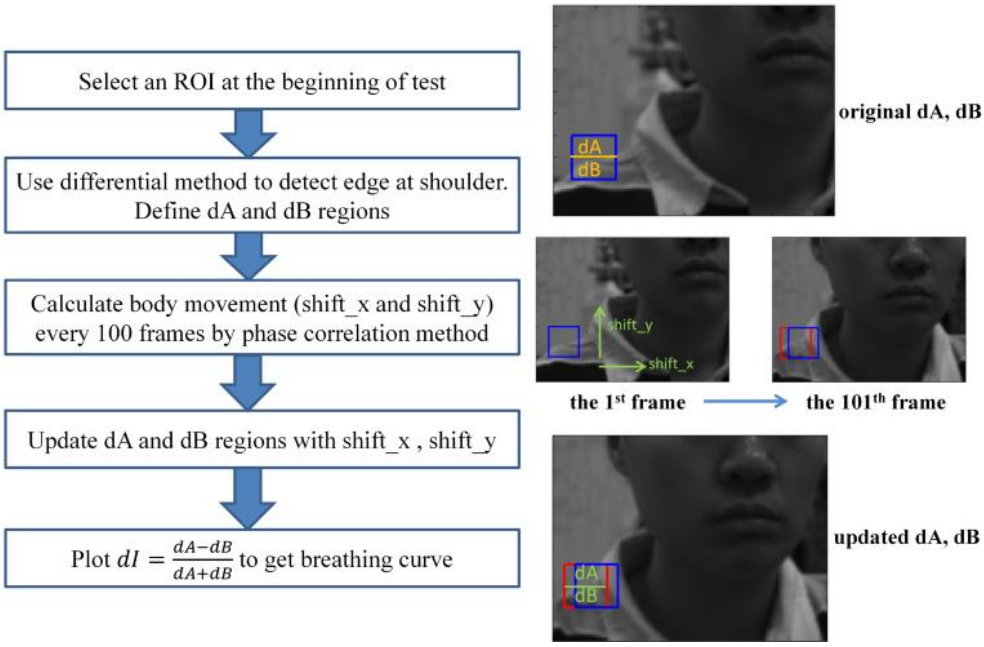

Figure 4-2 Motion Tracking Algorithm Workflow.

The presented motion tracking algorithm can also be applied to PPG measurement to help on correction of motion artifacts.

4.2 Breathing Pattern Monitoring

An example of breathing waveforms obtained with the method described in section 4.1 is shown in Figure 4-3 A region of 40 × 40 pixels around the edge of each shoulder was selected to be the ROIs for breathing detection (Figure 4-3) (left panel). The downhill cycles correspond to exhalation periods when the thoracic cavity is shrinking and the shoulders move downwards, whereas the uphill cycles correspond to inhalation periods when the thoracic cavity is expanding and the shoulders move upwards. The breathing patterns obtained from the left and the right shoulders are consistent with each other (Figure 4-3) (right panel).

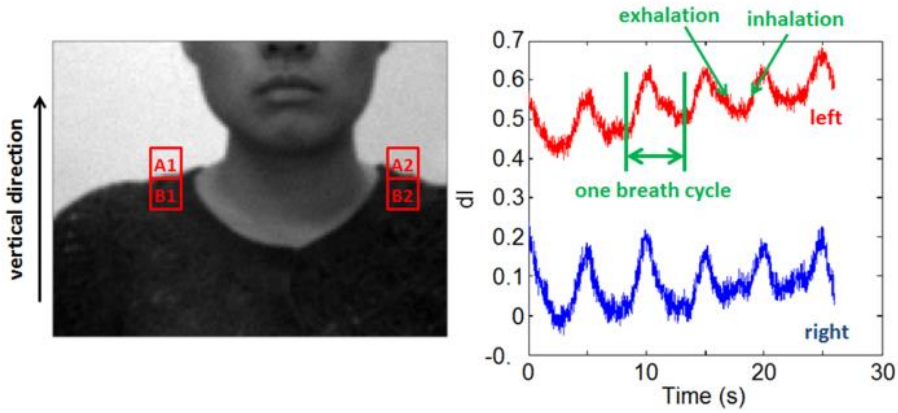

Figure 4-3 Breathing Pattern Detection by Shoulder Movement Tracking.
Left: An ROI is selected on each shoulder (red box), and each ROI is divided into two sub-regions, A and B, along vertical direction. Right: Corresponding breathing cycles from the ROIs using differential detection method.

To further demonstrate the reliability of the method for real-time monitoring of breathing pattern, the subject was instructed to change breathing pattern intentionally. Initially, the subject breathed normally for six cycles, followed by four cycles of deep breathing and then eight cycles of rapid breathing. The results shown in Figure 4-4

demonstrate that the presented method successfully captures the breathing pattern variations.

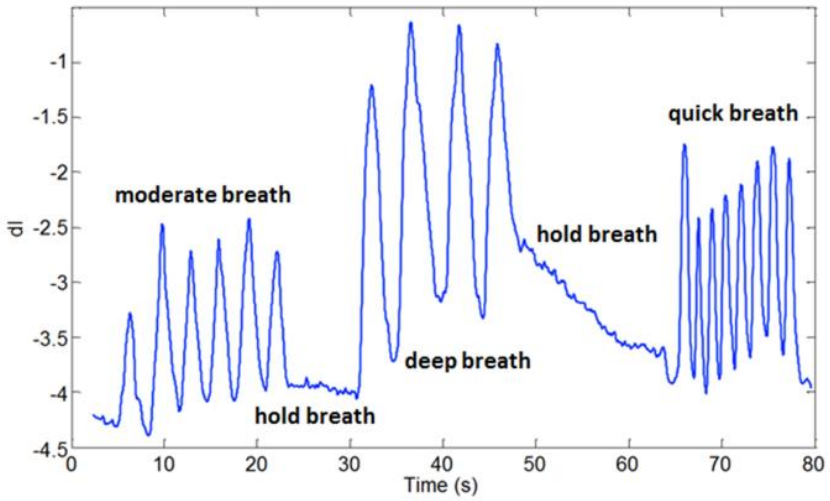

Figure 4-4 Obtained Different Breathing Patterns.

The effectiveness of the motion tracking algorithm is shown in Figure 4-5 (a), which compares the results with and without the motion tracking algorithm. Without applying the motion tracking algorithm, the measured breathing signal was overwhelmed by the body movement. In contrast, the breathing pattern was clearly observed after the implementation of the motion tracking algorithm. The algorithm worked effectively since the breathing-related body movement of the shoulders has small amplitude and is primarily in the vertical direction, which is different from the relatively large body movement that may occur in all directions and at different time scales from regular breathing.

Two reference technologies were used for validation and calibration, viz., a Zephyr wearable device and an Oxycon metabolic analysis instrument. The Zephyr device used a movement sensor integrated in a belt wrapped around the user's chest and reported user's breathing rate in BPM. Since the Zephyr device does not provide exhaled breath volume

data, the Oxycon instrument was used to measure both the breathing frequency (unit: BPM) and exhaled breath volume (unit: L) via a turbine flow meter attached to a mask worn by the user.

The breathing pattern measured with the presented image processing method results in signal waveforms that are consistent with those obtained using the reference devices Zephyr (Figure 4-5 (b)) and the Oxycon (Figure 4-5 (c)) devices in terms of both breathing frequency and relative breathing amplitude.

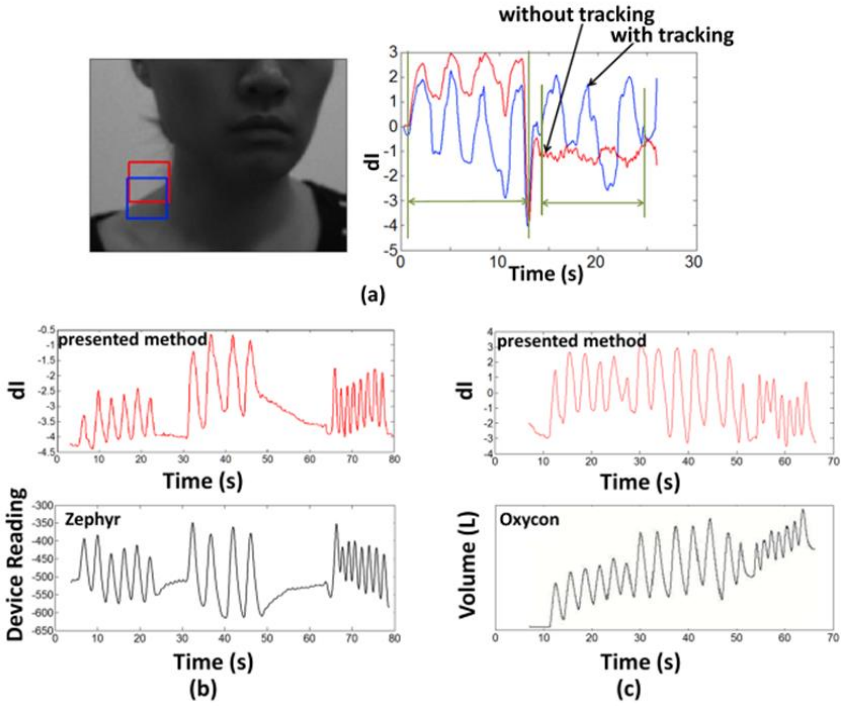

Figure 4-5 Respiration Monitoring with Reference Validations.
(a) Effectiveness of motion tracking algorithm for breathing pattern detection. Left: Image of a study subject with a selected ROI on the right shoulder. When the motion tracking algorithm is enabled, the ROI follows the body movement (blue box). In contrast, when the motion tracking algorithm is disabled, the ROI is fixed in the image and the shoulder may move out of the ROI (red box). Right: Breathing patterns with (blue curve) and without (red curve) the motion tracking algorithm. (b) Comparison of breathing patterns obtained with the presented method (red line) and Zephyr (black line). (c) Comparison of breathing patterns obtained with the presented method (red line) and Oxycon device (black line).

4.3 A Small-Scale Pilot Study for Breathing Rate and Heart Rate Detection

To demonstrate the robustness of the developed methods to monitor heart rate and breathing rate, a small-scale pilot study was conducted for statistical analyses. Ten subjects were enrolled in the IRB study approved by Arizona State University. The subjects were of different genders (6 males, 4 females), age (27.3 ± 4.5 years old, mean ± SD), ethnic profiles and skin colors. Informed consents were obtained from all subjects following approved protocol.

Bland-Altman plots were used to compare presented physiological signal detection methods with reference technologies. Figure 4-6 shows the Bland-Altman plot for heart rate detection. The differences between presented non-contact method and a commercial pulse oximetry (y-axis) were plotted against the average of the two methods (x-axis). The mean difference was 0.86 bpm with 95% limits of agreement (±1.96 standard deviation) at -2.47 bpm and 4.19 bpm. The root-mean-square error (RMSE) was 1.87 bpm and r was 0.98 ($p<0.001$). Figure 4-7 shows the Bland-Altman plot for breathing rate detection. The differences between presented non-contact method and Zephyr (y-axis) were plotted against the average of the two methods (x-axis). The mean difference was 0.02 breaths/min with 95% limits of agreement (±1.96 standard deviation) at -2.40 breaths/min and 2.45 breaths/min. RMSE was 1.20 breaths/min and r was 0.93 ($p<0.001$).

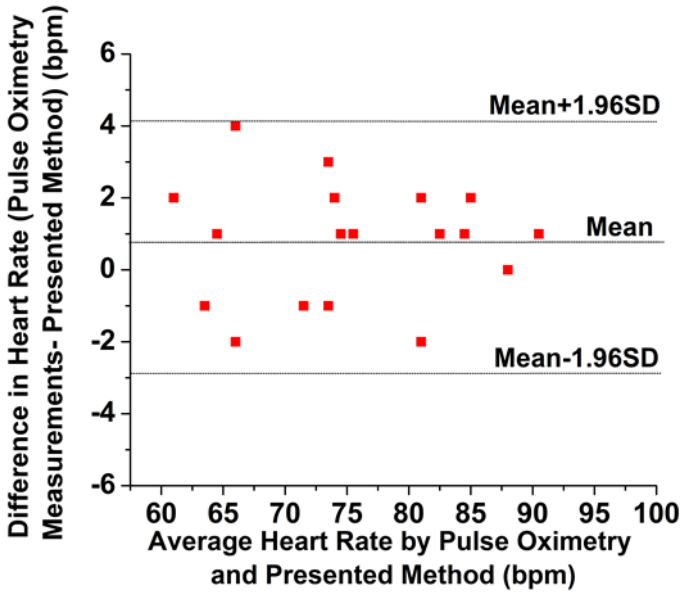

Figure 4-6 A Bland-Altman Plot for Heart Rate Monitoring Evaluation.
The plots shows the average of the heart rate measured with a commercial pulse oximetry and the presented method, plotted against the difference between them.

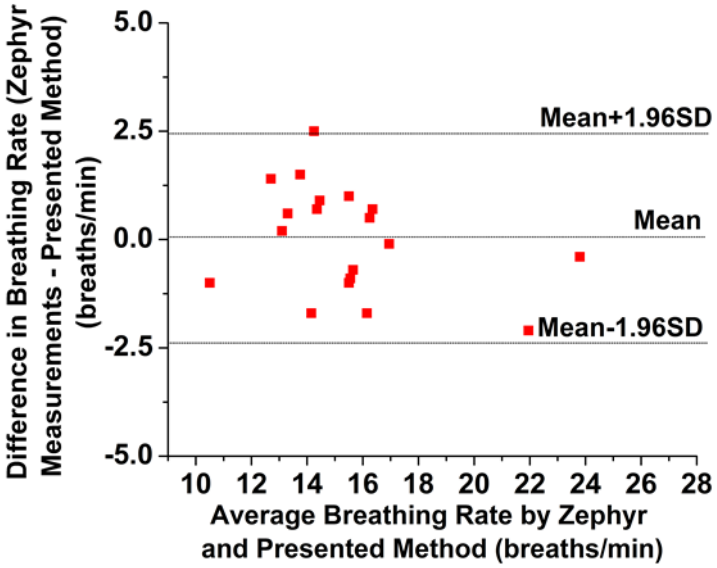

Figure 4-7 A Bland-Altman for Breathing Rate Monitoring Evaluation.
The plot shows the average of the breathing rate measured with a commercial device Zephyr and the presented method, plotted against the difference between them.

Both the presented method and the reference technologies can introduce errors in the test results. For statistical analyses, $p<0.05$ is considered to be a significant correlation between the two compared methods. I therefore concluded that the overall error rates were acceptable.

4.4 Determination of Exhalation Flow Rate

Exhalation flow rate is an important physiological parameter and proportional to a subject's metabolic rate [55]. Based on presented video-based method, the amplitude of the breathing-related shoulder movement is associated with the exhaled breath volume per breathing cycle, or VE. The relationship was examined by plotting the amplitude vs. exhalation flow volume obtained with the Oxycon instrument. Six tests were carried out, and in each test, the subject changed the exhalation rate. Figure 4-8 shows a plot of the breathing amplitude (from the differential signal, *dI*) of the tests vs. the exhaled breath volume obtained with the Oxycon instrument, which shows linear relationship (R^2 = 0.81) between *dI* and the exhaled breath volume.

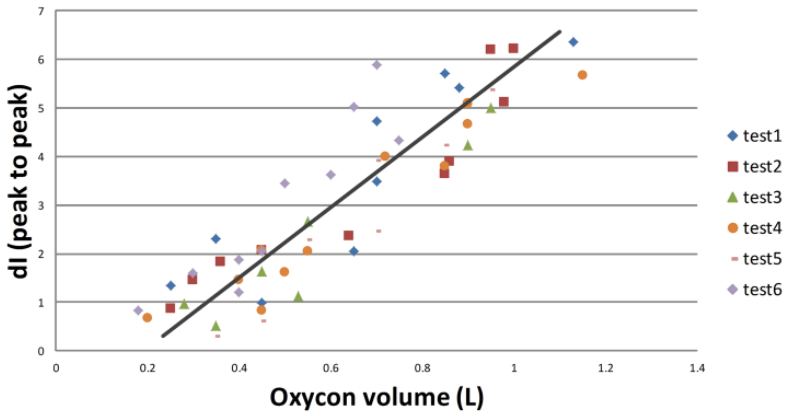

Figure 4-8 Correlation between the Exhaled Breath Volumes and Differential Signal.
Reference exhaled breath volumes are measured from a commercial device. In the presented method, the exhaled breath volume is taken from the shoulder movement, or *dI*. Data from six tests can be fit with a linear curve. For every unit of *dI*, the volume change is about 0.15 L.

The exhalation flow rate can be calculated as the exhaled breath volume divided by exhalation time (12),

$$exhalation\ flow\ rate = \frac{exhaled\ \ breath\ volume}{exhalation\ time} \quad (12)$$

This observation demonstrates a method to remotely determine exhalation flow rate under normal living condition.

4.5 Discussion

All of the experiments were all conducted with the subject sitting on a chair. The subject was allowed moderate movements. I anticipate challenges if the subject has significant movements, since it may be more difficult to isolate motions which are due to respiration activity and motions which are due to motion artifacts. However, I also believe that more accurate motion tracking algorithms can be created in the future to overcome the limitation of current method.

CHAPTER 5

NON-CONTACT BALLISTOCARDIOGRAM MONITORING

5.1 Ballistocardiogram Basic Concept and Traditional Measurement Methods

Ballistocardiogram (BCG) measures repetitive body motion caused by the cardiac contraction and ejection of blood during cardiac cycles. BCG waveform contains features that can indicate some physiological attributes [66, 67], and an irregular BCG may reveal abnormal circulation and cardiac diseases [68-71]. Typically, a BCG waveform consists of several waves, which are distinguished by shape, relative amplitude, and the sequence of occurrence. Each of these constituents is associated with a different cardiac event [72]. For instance, the "IJ wave" of acceleration BCG may be used to measure ejection force and stroke volume [68, 73-76]. An increase in IJ amplitude implies an increase in cardiac ejection, which can be used as a potential indicator of recovery in patients with heart diseases.

Starr introduced modern BCG in 1930s [66-68, 71, 76-79]. Traditionally, BCG measurements used table-based apparatuses, such as suspended bed [79], and suspended rigid platform [80]. Elliott et al. developed an electrochemical method to measure BCG [81]. These BCG apparatuses were bulky and hard to implement compared with other medical procedures, such as ECG, which led to a decline in the use of BCG after 1970s. With the development of new sensor technologies, BCG has attracted research interest again in recent years. An ear-worn device was demonstrated for ECG, BCG, and PPG monitoring [74, 82-84], where the BCG was obtained from an accelerometer integrated in the device. Other approaches used to measure BCG include weighing scale [23, 73, 85-87],

polypropylene film coated with electrically conductive layers [88, 89], and force sensor mounted in bed [90]. In addition to these acceleration and force measurements, displacement BCG was also obtained using a linear variable displacement transformer position sensor [91].

The aforementioned BCG monitoring methods require direct contact between the measuring instrument and subject, which is not always desirable. A non-contact video-based method can provide a more natural and comfortable way for BCG monitoring. Moreover, it is an MRI-safe measurement that can track the subject's cardiac activities in a changing magnetic field environment [92]. However, non-contact monitoring of BCG is not well established. Balakrishnan et al. [93] detected heart rate by tracking the vertical movement of head, but the full BCG features were not resolved. Krug et al. [92] used a camera to track the motion of a marker with moiré pattern worn by the subject on the nasal bridge. The subject also needed to wear a head coil fitted with a cushion to avoid motion artifacts.

In this thesis, a non-contact method is reported to monitor BCG using a camera without wearing any extra equipment or marker by the subject. The BCG measured using the presented non-contact method showed a similar waveform as that measured using direct body BCG system [78]. Furthermore, the method was validated by comparing the obtained BCGs with those recorded with an accelerometer worn by the subjects.

5.2 Design of Experiment and Data Acquisition

A Pike color camera (F-032C) was used to capture the video of a subject's face at a frame rate of 60 frames/second under indoor ambient light condition (Figure 5-1 (a)).

BCG acquisition is easily affected by various noise factors, such as respiratory activity and random body movement [66]. To minimize the latter, the subject was asked to lie down, face upward, on a yoga mat at a distance of approximately 0.5 m from the camera lens. Based on current experiment setting, one pixel in the captured image is equivalent to approximately 1×10^{-4} m on the subject's face. The video was recorded for 30 seconds in each experiment. The first ten seconds of the video are discarded during processing, since that is the amount of time it takes the camera to ramp up to the desired stable frame rate of 60 frames/second.

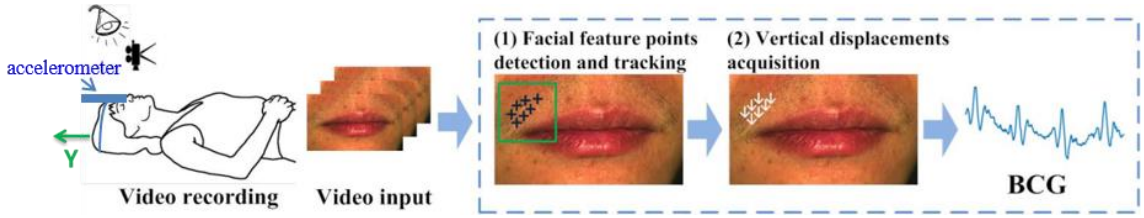

(a)

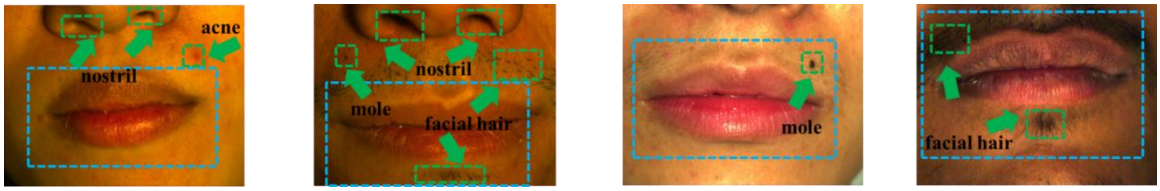

(b)

Figure 5-1 Overview of the Method.
(a) Video recording and flowchart of the presented BCG monitoring method. (b) ROIs and related facial features for BCG detection are highlighted in green with arrows. Related facial features are annotated in sample images.

For BCG detection, an ROI was selected, including at least one facial feature. For each subject, based on his or her personal characteristics, it was found that multiple options of the facial feature could be used to track BCG. Examples of the features that have

successfully used include mole, facial hair, nostril, acne, and skin pigmentation. The BCGs from different facial features on the same subject were similar (Figure 5-3).

Mouth, and its surrounding area, was selected as the ROI due to the availability of abundant distinct facial features for BCG tracking (Figure 5-2 (b)).

5.3 Signal Processing

Feature points in the defined ROI were detected from the first frame of the video based on the method proposed by Shi et al. [94]. The motion of each detected feature point was tracked over video frames with the Kanade-Lucas-Tomasi algorithm (KLT) [95, 96]. For an affine motion field

$$\delta = Dx + d, \quad (13)$$

where d is the translation of the feature window's center and D is the deformation matrix, which is given by

$$D = \begin{bmatrix} d_{xx} & d_{xy} \\ d_{yx} & d_{yy} \end{bmatrix}. \quad (14)$$

KLT determines the motion parameters D and d that minimize the dissimilarity ε between two adjacent frames, viz. I and J, in a given feature window around position x. ε is expressed as

$$\varepsilon = \iint_W \left\{ J\left[(1+D)x + d\right] - I(x) \right\}^2 w(x) dx, \quad (15)$$

where $w(x)$ is the weighting function.

The vertical displacement (in the direction along feet to head) contains BCG [82, 92], which was analyzed in detail. To convert the feature dimensions represented in terms of the number of pixels into meters, a conversion factor was defined as

$$\alpha = \frac{\text{feature\_dimension}(m)}{\text{feature\_pixel\_number}(pixel)}. \quad (16)$$

This conversion factor was determined by measuring facial feature dimension (e.g., mouth) using a ruler and counting the pixel numbers of the corresponding feature in the image.

For each frame, n, the vertical components of point locations, y_i, were averaged over all the detected feature points, and plotted against time to provide displacement BCG_d, which can be written as

$$BCG_d(n) = \frac{\sum_{i=1}^{k} y_i(n)}{k} \times \alpha, \quad (17)$$

where k is the number of detected feature points and may vary depending on the type of facial feature.

The first and second temporal derivatives of the displacement BCG were then calculated, leading to velocity BCG_v and acceleration BCG_a, respectively.

Several features were extracted from measured BCG waveforms, including ensemble averages, IJ intervals and amplitudes. Ensemble averaging was performed over the obtained waveforms to look into the morphology of these signals. In order to obtain the ensemble average, the 20 seconds duration signal was plotted as an eye diagram over one cardiac cycle. Multiple individual cycles (~ 20 beats) were aligned and then averaged to obtain an ensemble waveform. This is similar to the methods reported in literature [84, 85] to analyze BCG. A time duration of 20 seconds results in adequately stable ensemble waveform [84]. IJ interval was calculated as the time difference between acceleration BCG

I_a peak and J_a peak in the same beat, while IJ amplitude was the absolute value of the amplitude from I_a peak to J_a peak.

Compared to PPG, BCG frequency components are more complex and have a wider distribution in the spectrum (Figure 5-2 (d)). The majority of BCG power stays in the range of 1 - 10 Hz [84, 88]. Therefore, the SNR of BCG was evaluated based on two methods: one of them employing maximum likelihood and the other using sample correlation coefficient [85, 97].

SNR estimation based on maximum likelihood can be obtained by:

$$SNR_{ML} = \frac{2\sum_{i=1}^{N} EA_{sub,1}(i)EA_{sub,2}(i)}{\sum_{i=1}^{N}(EA_{sub,1}(i) - EA_{sub,2}(i))^2}, \quad (18)$$

where $EA_{sub,1}$ is the sub-ensemble average for the first ten seconds of the measured displacement BCG, and $EA_{sub,2}$ is that for the remaining ten seconds. N is the number of samples in the sub-ensemble averages, and i is the sample time index.

Another SNR estimation method is based on sample correlation coefficient r:

$$r = \frac{\sum_{i=1}^{N} EA_{sub,1}(i)EA_{sub,2}(i)}{\sqrt{\sum_{i=1}^{N} EA_{sub,1}(i)^2 \sum_{i=1}^{N} EA_{sub,2}(i)^2}}. \quad (19)$$

The SNR can be then calculated as:

$$SNR_r = A\frac{r}{1-r} + B, \quad (20)$$

where A and B are given by:

$$A = \exp(\frac{-2}{N-3}), \quad (21)$$

$$B = -\frac{1}{2}(1-\exp(\frac{-2}{N-3})), \quad (22)$$

5.4 Detected BCG Waveforms

Figure 5-2 shows the BCG waveforms obtained from a video with a male subject. The J_d-peak, one of the most prominent features of BCG, is clearly resolved in the displacement BCG obtained with the presented video method (Figure 5-2 (a)). The corresponding velocity and acceleration BCGs were obtained by taking first and second temporal derivatives first, and then filtered with a 2nd order Butterworth filter with a passband of [0.5, 10] Hz (Figure 5-2 (b) and Figure 5-2 (c)). DC bias is removed from these signals. Ensemble averages of these waveforms are provided on the right of the figures. The power spectra of the displacement BCG are shown in Figure 5-2 (d).

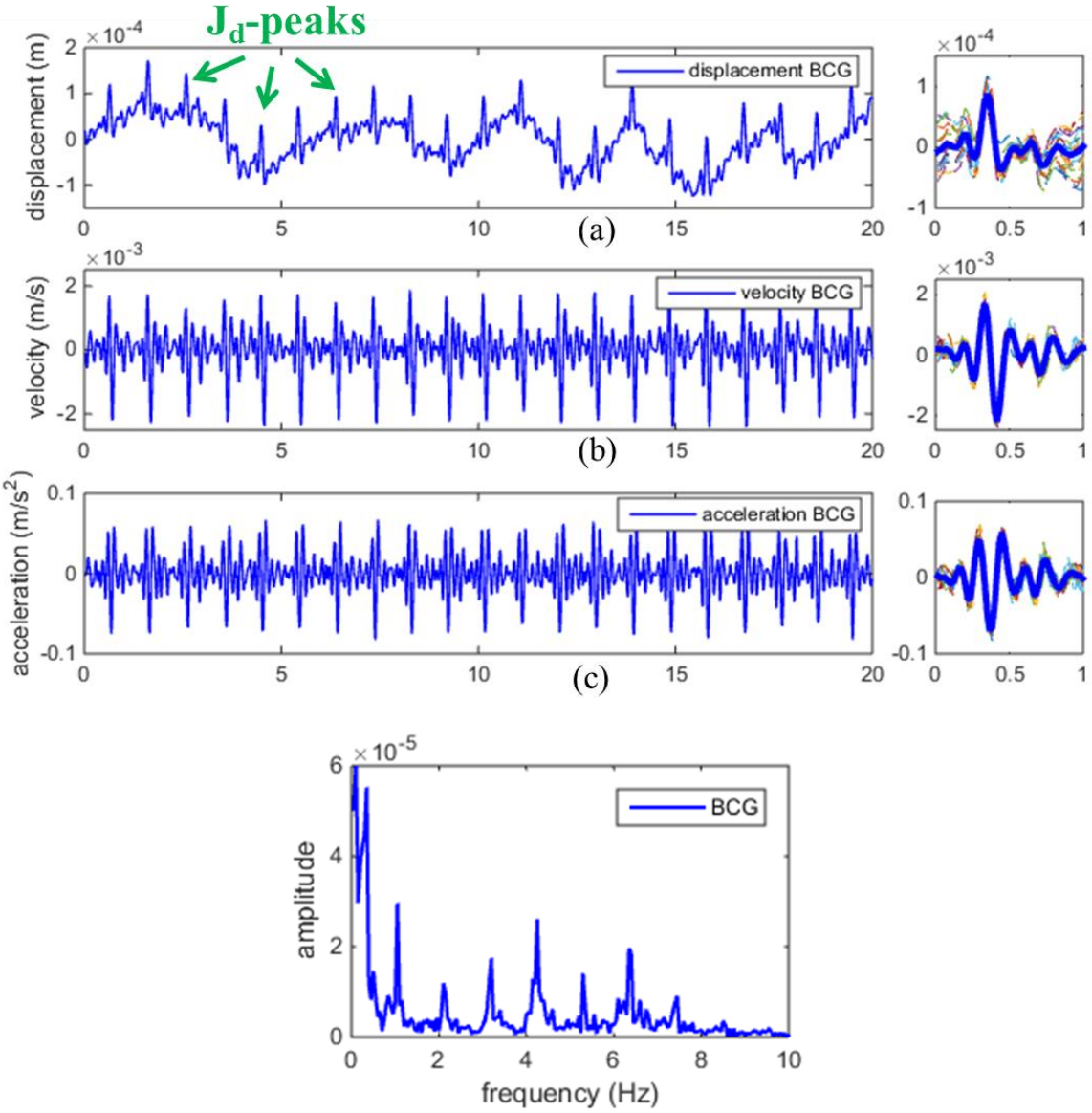

Figure 5-2 Detected BCG Waveforms.
(a) Displacement BCG. (b) Velocity BCG. (c) Acceleration BCG. (d) Displacement BCG frequency spectrum.

Figure 5-3 shows the BCGs detected from three different facial features (facial hair, mole and nostril) using the same video of a male subject. BCGs obtained from different features look very similar. The Pearson's linear correlation coefficients between every two

signals are larger than 0.95, implying that the displacement BCGs obtained from the three features are strongly correlated.

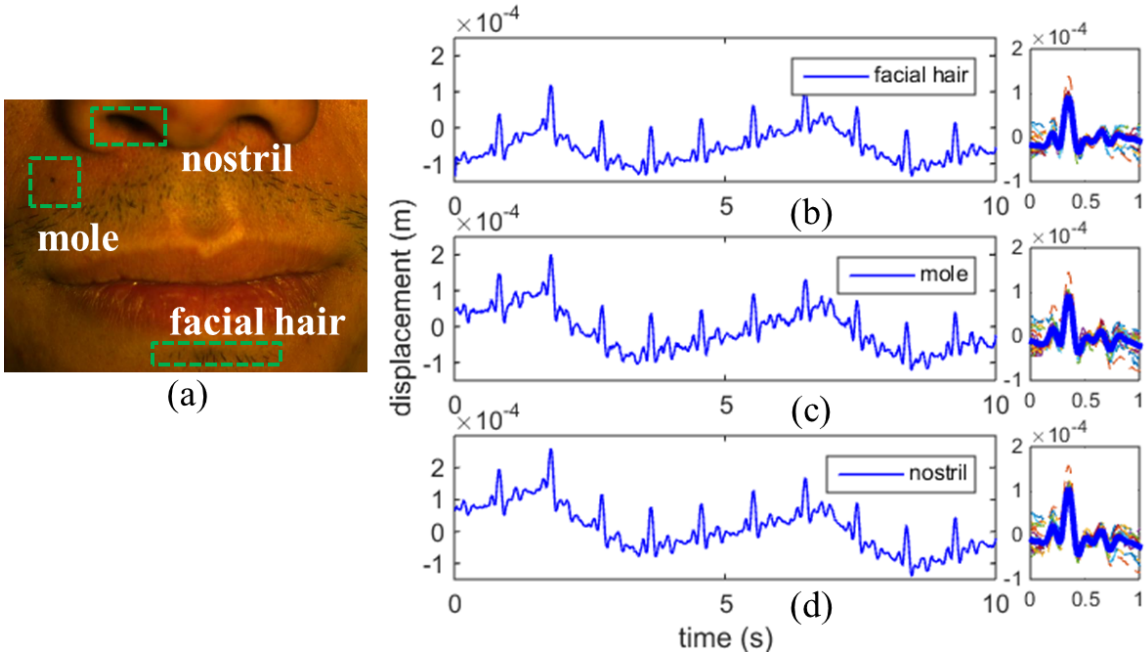

Figure 5-3 BCG Waveforms Detected from Different Facial Features.
(a) Video sample and three different facial features (facial hair, mole and nostril). (b) BCG detected from mole. (c) BCG detected from facial hair. (d) BCG detected from nostril. Corresponding ensemble averages of the waveforms are on the right.

5.5 Reference Validation

To validate the presented BCG detection method, I compared the measured BCG waveforms against those in literature [78, 98], and also carried out BCG measurement simultaneously with the accelerometer, which is a well-accepted method for acceleration BCG monitoring [74, 82, 83, 99]. The accelerometer (LSM330) used for the purpose of this study is that found in a commercial off-the-shelf Samsung S4 smartphone. The sample rate of the accelerometer is set at 50 Hz, and based on the datasheet, the linear acceleration sensitivity is typically around 0.007 m/s^2. The noise level is about 0.005 m/s^2, which is estimated from the standard deviation by keeping the smartphone stationary on a flat

surface for 30 seconds. For measurements with test subjects, the smartphone was placed on the subject's forehead and held in place with a rubber band (Figure 5-1 (a)). The y-axis (feet-head direction) acceleration measured by the accelerometer was compared to the vertical acceleration BCG obtained using the presented method. The Pearson's linear correlation coefficients between ensemble averages, IJ amplitudes and intervals obtained using the two methods were calculated.

The acceleration BCGs along feet-head direction obtained using the presented, and the reference methods are plotted in Figure 5-4. Both waveforms are filtered with a 2^{nd} order Butterworth filter with a passband of [0.5, 10] Hz. The obtained BCG waveform from the video is resampled from 60 Hz to 50 Hz to match the sampling rate of the accelerometer for comparison purpose. The overall patterns and the obtained cardiac cycles from the two methods are consistent with each other, which validates the presented non-contact method for BCG monitoring.

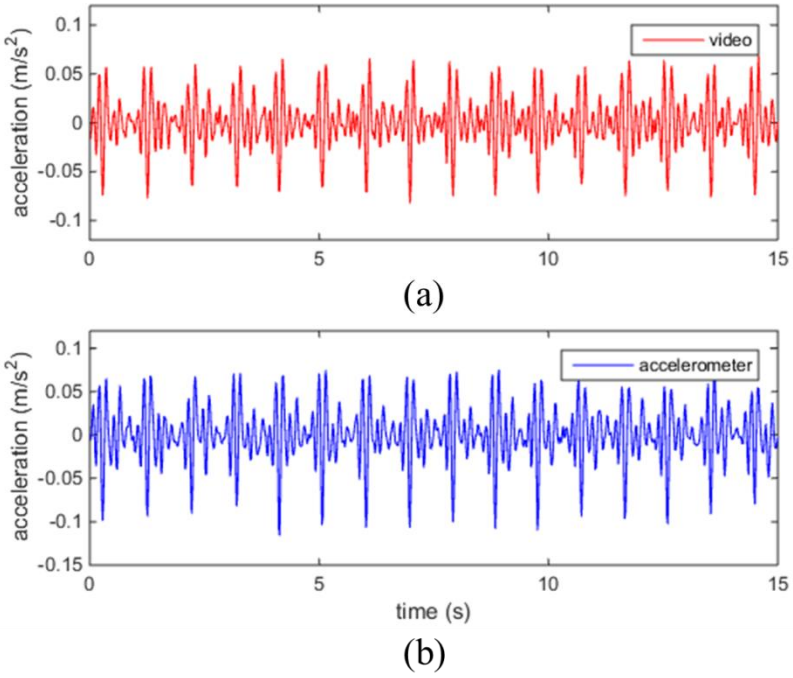

Figure 5-4 BCG Validation.
(a) Vertical acceleration from video. (b) Vertical acceleration from accelerometer.

To further examine the detailed features of the BCGs obtained with the two methods, ensemble averaging was performed for two subjects over a duration of 20 seconds, and the resulting waveforms, including individual cycles (dash lines) and ensemble averages (solid lines), are shown in Figure 5-5.

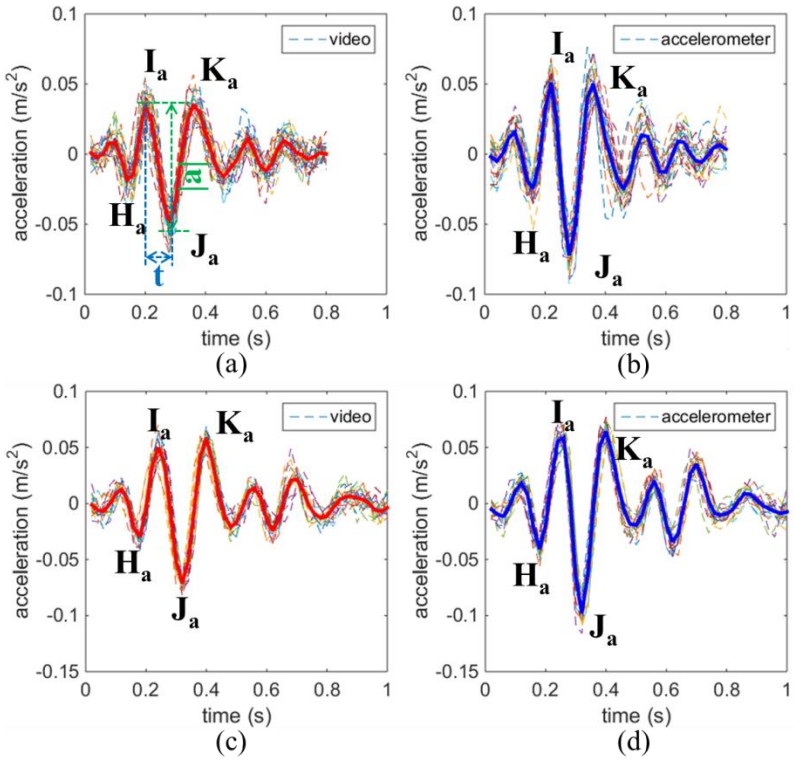

Figure 5-5 Comparison of Acceleration BCG Waveforms.
BCGs obtained with the presented non-contact method and reference method over 20 seconds. (a) BCG waveforms, for a female subject (heart rate = 1.3 Hz), measured from 25 individual cardiac cycles (dash lines) and ensemble average for the 25 cycles (solid line). The major waves (H, I, J, and K), IJ amplitude (|*a*|), and IJ interval (*t*) are denoted with letters. (b) BCG for the female subject in (a), measured simultaneously using an accelerometer. (c) BCG waveforms, for a male subject (heart rate = 1.1 Hz), measured from 19 individual cardiac cycles (dash lines) and ensemble average for the 19 cycles (solid line). (d) BCG for the male subject in (c), measured simultaneously using an accelerometer.

For both subjects, the major peaks in BCG waveforms from the presented and reference methods are similar, and the Pearson's linear correlation coefficients are larger than 0.95, implying that the test results obtained from the two methods are strongly correlated. Furthermore, the obtained BCGs from both methods are also consistent with the typical direct body measurement BCG waveforms reported in literature [78, 99].

5.6 Small Scale Pilot Study

A small-scale pilot study was carried out to demonstrate the presented video-based method for monitoring BCG. The study included 23 subjects (approved by Institutional Review Board at Arizona State University, No. STUDY00003483). The subjects included 15 males and 8 females of different ages (29 ± 5 years old, mean ± SD) and ethnic profiles, and from different geographic regions (North America, South America, East Asia and South India). The skin colors of the subjects ranged from type II (white) to type V (brown) based on the Fitzpatrick scale [100]. Informed consents were obtained from all the subjects following an approved protocol. None of the subjects had any known cardiovascular disease.

In the small-scale pilot study, I performed the test as described in previous section on each subject. Figure 5-6 shows the displacement BCGs obtained from seven different subjects for the purpose of demonstration. The overall BCG waveforms are similar for all subjects, but the detailed features show substantial variations due to different physiological attributes, which have also been reported by other literatures [85, 101, 102]. The largest amplitudes of the measured displacement BCG J-peaks ranged from 1×10^{-4} to 2×10^{-4} m. The velocity and acceleration peaks varied from 2×10^{-3} to 6×10^{-3} m/s, and 0.05 to 0.15 m/s^2, respectively. These values are comparable to those reported by other researchers using different methods (Table 5-1). For the same subject, the measurement error for these values was about 10% in consecutive tests.

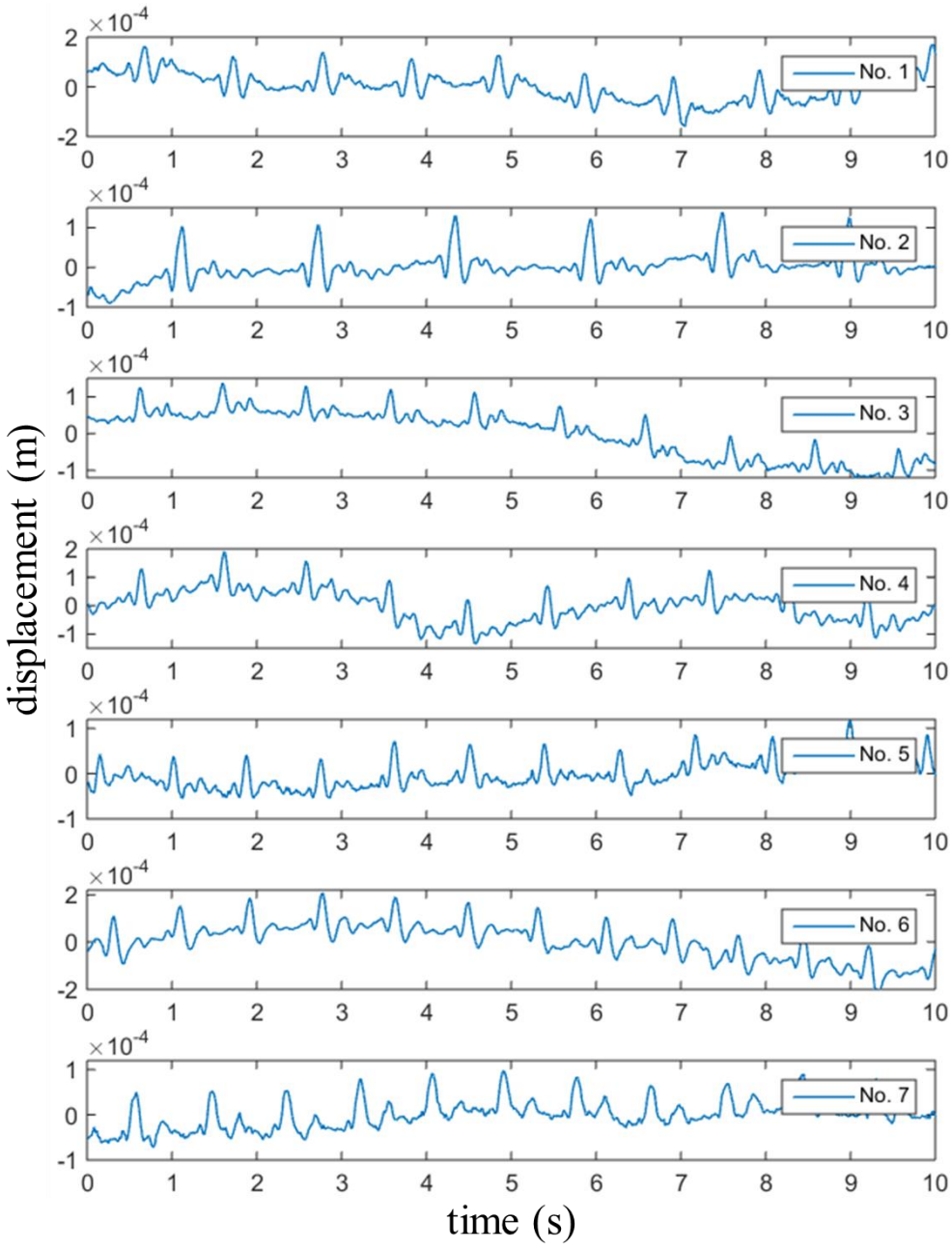

Figure 5-6 Displacement BCGs Obtained from Different Subjects.

Table 5-1
BCG Values Comparison.

BCG Type	References	Presented Method
displacement (m)	6×10^{-5} [28], 1.5×10^{-4} [50], 10^{-4} [45]	1.5×10^{-4}
velocity (m/s)	2.5×10^{-3} [28]	4×10^{-3}
acceleration (m/s^2)	0.1 [9, 17], 0.08 [45]	0.09

The reference values are estimated from the reported test results (plots).
The values from the presented method are averaged over 23 healthy subjects.

I compared the IJ amplitudes ($|a|$) and intervals (t) of acceleration BCGs determined using the presented method with those using the reference accelerometer. Figure 5-7 and Figure 5-8 show the plots of these two values from 73 tests with linear least square regression. Good linear correlation is found between the presented and reference methods for both plots ($R^2 = 0.82$ and $R^2 = 0.7$). The difference between the two methods may be attributed to different body locations (mouth region for presented method and forehead for accelerometer). The accuracy may also be affected by the calibration error.

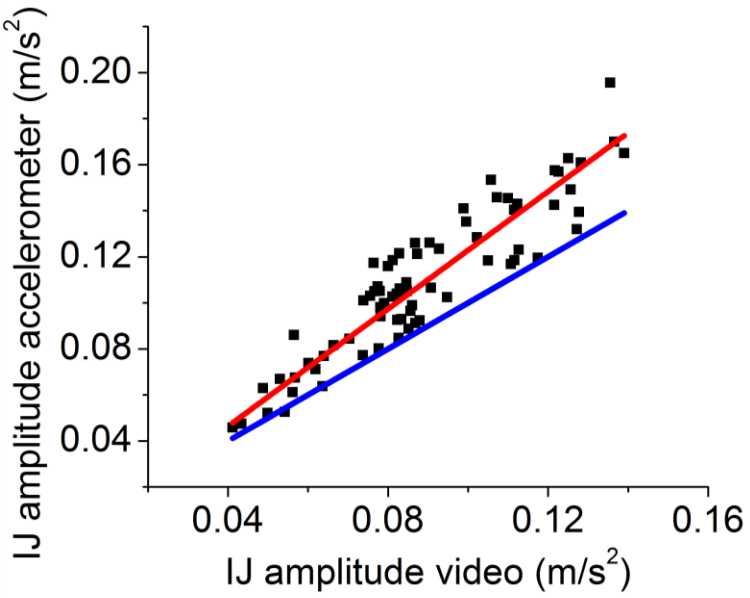

Figure 5-7 IJ Amplitude Comparison between Two Methods.
Correlation between the IJ amplitudes of acceleration BCGs obtained using the presented and reference methods. The red line is a linear fit of the scattered data. The blue line is the identity line (slope = 1).

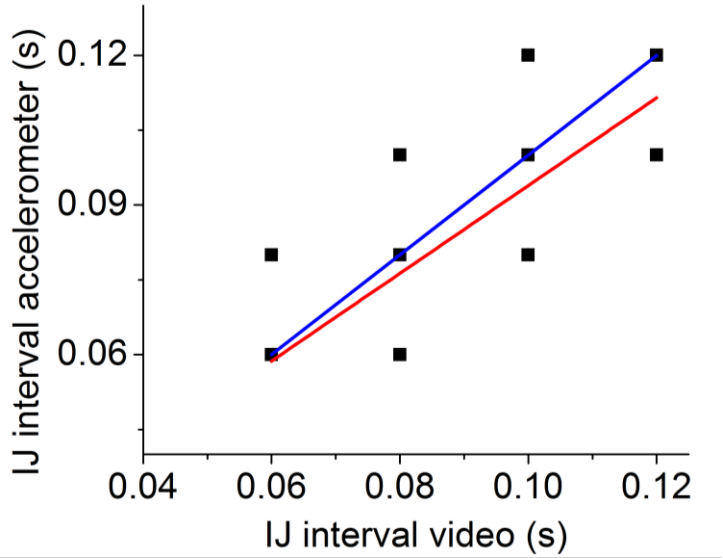

Figure 5-8 IJ Interval Comparison between Two Methods.
Correlation between the IJ intervals of acceleration BCGs obtained using the presented and reference methods. The red line is a linear fit of the scattered data. The blue line is the identity line (slope = 1). The plot has overlapping data points.

Figure 5-9 summarizes the Pearson's linear correlation coefficients between the BCGs measured using the presented method and reference accelerometer. Figure 5-10 shows the BCG SNR values based on maximum likelihood (8) and sample correlation coefficient (10) using the presented method. All the test results are divided into four groups based on the types of facial features used for motion tracking. The SNR values and the standard deviations are comparable to those in [20] using weighing scale. Figure 5-9 and Figure 5-10 suggest that the selection of facial features is not a key factor for video-based BCG monitoring since the values are comparable among different features.

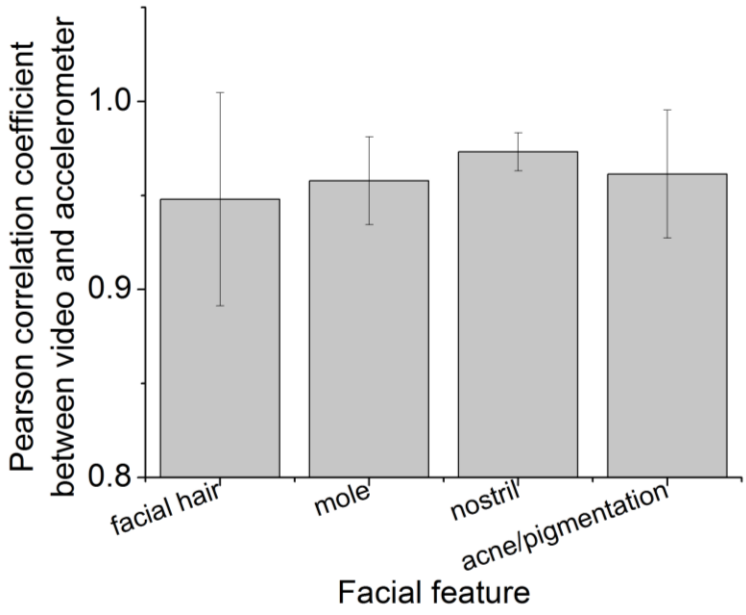

Figure 5-9 Pearson Correlation Coefficients between Two Methods.
Analysis is based on different facial features.

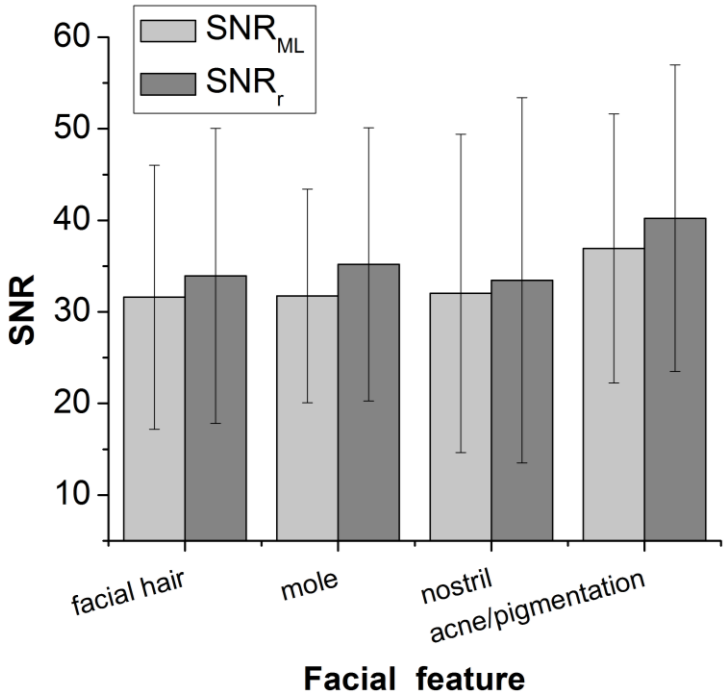

Figure 5-10 SNR Estimation of BCG.
SNR estimation using the presented method, with standard deviation, based on maximum likelihood (SNRML) and sample correlation coefficient (SNRr).

5.7 Signals from Other Posture

The presented method was also validated against sitting position. Figure 5-11 shows the signals obtained when the subject was sitting on a chair. BCG was obtained by tracking facial feature (mole) and PPG was obtained from the mouth region, using the same methods as described in the previous section. The subject was the same as the one in Figure 5-11. Accelerometer was also used as reference device for comparison. The Pearson's linear correlation coefficient between the presented method (Figure 5-11 (c)) and reference device (Figure 5-11 (d)) is 0.97. BCG waveforms show difference between sitting and supine positions, which has also been reported in other literature [25].

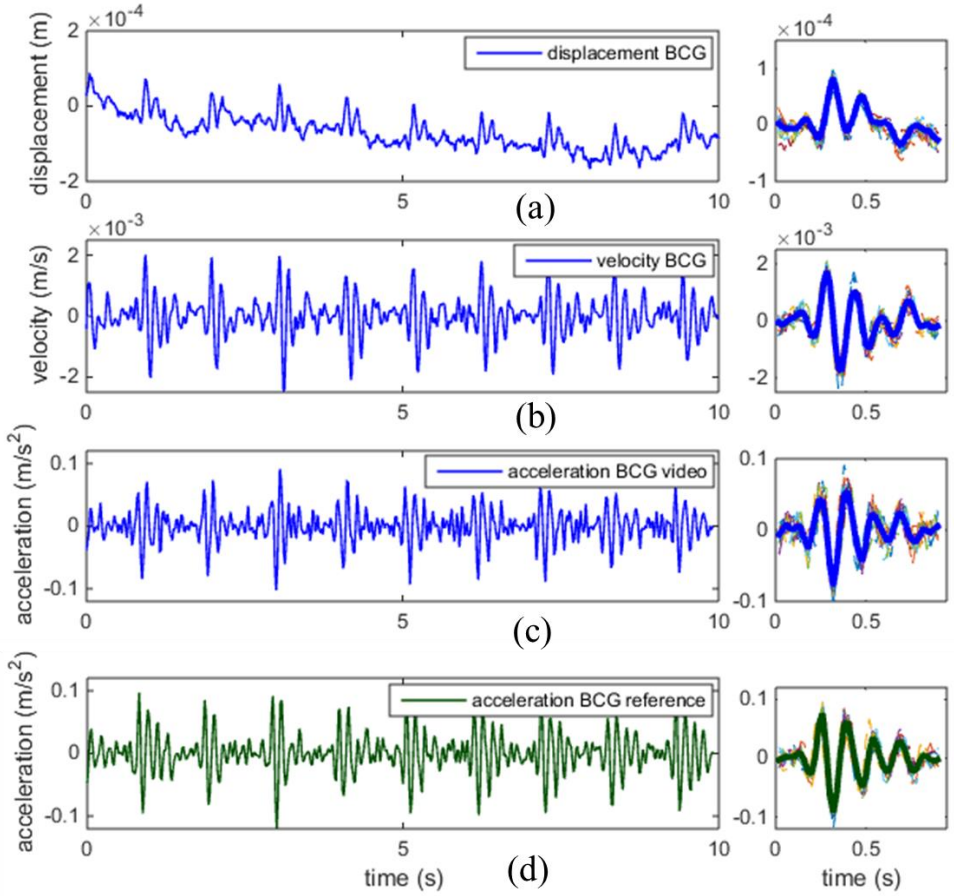

Figure 5-11 BCG Waveforms with a Sitting Position.
(a-d) Detected signals (on the left) with corresponding ensemble averages (on the right). (a) Displacement BCG. (b) Velocity BCG. (c) Acceleration BCG from video-based method. (d) Acceleration BCG from reference device.

5.8 Discussion

The selection of facial features is not critical for BCG monitoring, but sharp focus of facial features in the video is beneficial for accurate tracking of BCG. Compared to supine position, sitting position is more easily affected by motion artifacts, since the body is more prone to involuntary movement in the latter posture due to an absence of support that is typically afforded in the former posture.

Future works will also include clinical studies with more subjects, especially those with abnormal cardiovascular functions, which will help relate BCG features to physiological conditions of the subjects, and further validate the clinical value of the presented technique. If faster frame rate could be reached in the future, it will be beneficial for analyzing the high frequency features and the timing characteristics of the signals

CHAPTER 6

NON-CONTACT BLOOD PRESSURE MONITORING

6.1 Blood Pressure Monitoring Based on Cardiac Signals Timing Analysis

Different approaches have been attempted towards cuffless blood pressure (BP) measurement. MEMS devices, such as accelerometer [103] and conducting polymer actuator [104], have been implemented for this purpose. In addition, optical methods which are mainly based on utilization of pulse transit time (PTT) estimation have also been reported. PTT can be regarded as the relative timing between proximal and distal waveforms indicative of the arterial pulse [105], or the time interval for the pulse signal to travel between two body sites. Most published PTT-based BP monitoring studies look into the time difference between ECG and PPG signals [24, 106]. There are also studies on PTT acquisition based on PPG time delay between two body parts [14]. Some patents also describe similar ideas. In [107], a camera is used to capture blood volume pulses from subject's face, hand or foot, and the PTT can be extracted to determine relative BP. In [108], the inventors claimed to use the front and back cameras on the smartphone to get PTT for the same purpose. Kim etc. [23] demonstrated BCG can be used as proximal timing reference for cuffless BP measurement. A merit of BCG is that it can be measured at a distal location [105] (e.g., head, feet, wrist). Pinheiro etc. [109] has shown a correlation between the PTT obtained from ECG and PPG, and the PTT obtained from BCG and PPG. Researchers [86, 87, 110, 111] used weighting scale to measure BCG and ECG, and showed that the time interval between ECG "R" peak to BCG "J" peak is strongly correlated with cardiac pre-ejection period and systolic blood pressure. In other published

works which are related to BP monitoring based on BCG, Chen etc. [112, 113] presented a method to monitor BP based on BCG obtained from microbending fiber sensor, together with PPG obtained from a contact-based finger probe. These studies suggest BCG as a potential alternative pulse signal to measure PTT for estimating.

Non-contact monitoring BP using PTT-based methods can track the fast and transient changes in BP, which are difficult to obtain by traditional cuff-based method. These are also suitable for long term monitoring, since the users do not need to wear any extra device during the measurement.

6.2 Relationship between Pulse Transit Time and Blood Pressure

The relationship between PTT and BP can be assumed based on two models: arterial wall model and arterial wave propagation model [105]. If the arterial vessel model is simplified as an elastic cylindrical tube, then PTT can be regarded as the time to travel along the tube over a distance *l*. PTT and the internal pressure of the tube *P* are inversely related, and the relationship can be expressed as

$$PTT = l\sqrt{\rho C / A}\,. \quad (21)$$

where ρ is blood density, A is vessel cross-sectional area, and C is compliance, which represents the ability of vessel to distend and increase volume with increasing transmural pressure or the tendency of a vessel to resist recoil toward its original dimensions on application of a distending or compressing force [114].

Based on the simplified model, blood pressure P can be expressed with respect to PTT by

$$P = P_1\sqrt{\frac{A_m \cdot \rho \cdot l^2}{\pi A \cdot P_1 \cdot PTT^2} - 1} + P_0 \text{, (22)}$$

where A_m , P_0 and P_1 are subject-specific parameters [105, 115]. If assuming the values of the parameters based on reference [115], an inverse correlation can be found between PTT and BP in Figure 6-1.

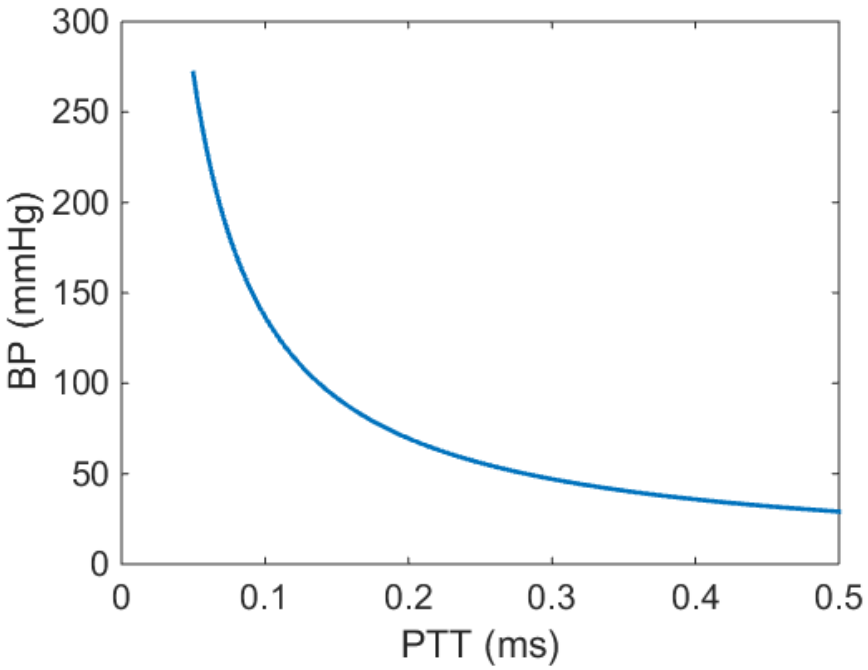

Figure 6-1 Relationship between PTT and BP.
The simulation is obtained based on (22) using parameters from [115] (P_1 = 1.8 mmHg, A_m = 0.011 cm^2, ρ = 1.06 g/cm^3, l = 10 cm, A = 2.77 cm^2, P_0 = 2.2).

Other researchers have also reported that BP can be empirically correlated with PTT with equations such as:

$$BP = K_1 \ln(PTT) + K_2 \text{, (23)}$$

$$BP = \frac{K_1}{PTT} + K_2 \text{, (24)}$$

$$BP = \frac{K_1}{(PTT - K_2)^2} + K_3, \quad (25)$$

where K_i (i = 1, 2, 3) are subject-specific parameters [105]. Therefore, it is expected that BP and PTT show correlation.

6.3 Method of Measurement

I used a Pike camera (F-032C) to monitor PPG and BCG. Mouth, and its surrounding area, was selected as the ROI due to the availability of abundant distinct facial features for BCG tracking. The PPG signal obtained from this ROI was also satisfactory. The camera setting was overall similar as the one in Figure 5-1. Meanwhile, I used EPIC Sensors (PS25451) to monitor ECG as a reference cardiac signal. Prominent features of these signals were identified by the time they occurred in each cardiac cycle. The features included: ECG "R" peak, PPG peak, and displacement BCG "J_d" peak. I further estimated the time difference between every two signals in each cardiac cycle, which included: (1) PTT_1: time delay from displacement BCG "J_d" peak to PPG peak; (2) PTT_2: time delay from ECG "R" peak to displacement BCG "J_d" peak; and (3) PTT_3: time delay from ECG "R" peak to PPG peak. The obtained time delays were plotted against time. Within these values, PTT_1 can be obtained by using just the camera. The obtained PTT values were averaged every ten seconds to reduce the influence of artifacts (e.g. respiration). A commercial cuff-based blood pressure monitor (Omron BP786) was used as reference to record BP values about every 40-50 seconds. The measurement error of the reference BP monitor is about ± 5 mmHg.

6.4 Design of Experiment

To validate the presented method for blood pressure tracking, the subjects were asked to do exercises to alter their blood pressure. Researchers have reported that systolic blood pressure (SBP) is inversely correlated with PTT after exercise [116]. Depending on the effort level and body condition of the subjects, SBP changed from 5 to 30 mmHg, and diastolic blood pressure (DBP) changed from 1 to 10 mmHg. Based on literature, SBP correlates better with PTT compared to DBP [24, 106].

Each experiment had five stages including 400-second video recording. The five stages were as follows:

- Stage I: System setup (120 seconds). The subject was asked to lie down and keep relaxed. Camera was adjusted to a proper view with good focus for video recording. Two ECG electrodes were in contact with the skin. Reference BP monitor was attached to subject's upper arm through a cuff.
- Stage II: Resting 1 (100 seconds). Video and ECG data were recorded simultaneously. Reference BP monitor measured the BP values every 40-50 seconds.
- Stage III: Exercise (60 seconds). The subject was asked to perform moderate exercise (sit up or push up) for about 1 minute.
- Stage IV: Re-setup (20-60 seconds). The subject was asked to lie down and relax. Camera, ECG sensors, and reference BP monitor were set up again to measure corresponding values from subject after exercise. The re-setup time was to be as

short as possible to capture BP recovery after exercise. It typically took about 20-60 seconds.

- Stage V: Resting 2 (~200 seconds). The system resumed data collection until the end of the experiment.

Due to the intense body motions in Stages III and IV, data recording (including video, ECG and reference BP) were not performed during these two time periods. The estimated changes in BP and PTT in different stages are illustrated in Fig 6-2.

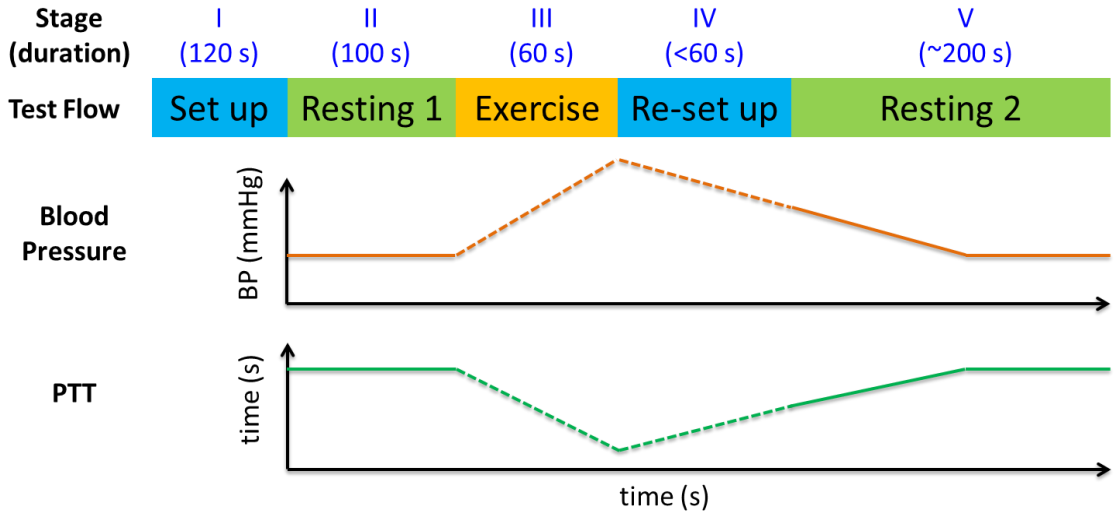

Figure 6-2 Experiment Workflow and Estimated Changes in BP and PTT.

6.5 Blood Pressure Tracking Results

Figure 6-3 shows the blood pressure tracking results and correlations with SBP measured by reference technology with a male subject (#1). Obtained PTT values were averaged every 10 seconds to reduce the influence of artifacts (Figure 6-3 (a-c)). SBP and DBP values were obtained from reference BP monitor every 50 seconds. The timing of the BP values was obtained when the BP readings were available on the device display. The shadowed areas indicate the time periods during which measurements were unavailable

due to exercise or waiting for system setup (Figure 6-3 (a-e)). Correlations are calculated between PTT values and SBP during BP recovery period after exercise (Figure 6-3 (f-h)). The SBP values are interpolated to reach a time resolution of ten seconds. In regular cuff-based BP device, SBP value is obtained earlier than DBP. Therefore, SBP was shifted in time by 20 seconds to compensate for this delay. Outliners, which may be caused by different sources of artifacts, such as unwanted body motions, or slow reference device response, were removed. The SBP increase due to exercise in this experiment was about 10 mmHg.

Correlation between blood pressure (especially SBP) and PTT values can be seen from all the plots in Figure 6-3 (a-c). The trends are clearer with Figure 6-3 (a) and Figure 6-3 (b). After exercise, the PTT values were lower than those before exercise. A quick recovery can be noticed right after the exercise, followed by a slow ascent. Among the three calculation methods, using PTT from PPG to BCG to track blood pressure, is the main interest of this work since both PPG and BCG waveforms can be obtained with a single camera simultaneously [117].

Figures 6-4 to 6-8 are the experimental results following the same protocols obtained from male subjects #2, #3, and female subjects #4, #5, #6.

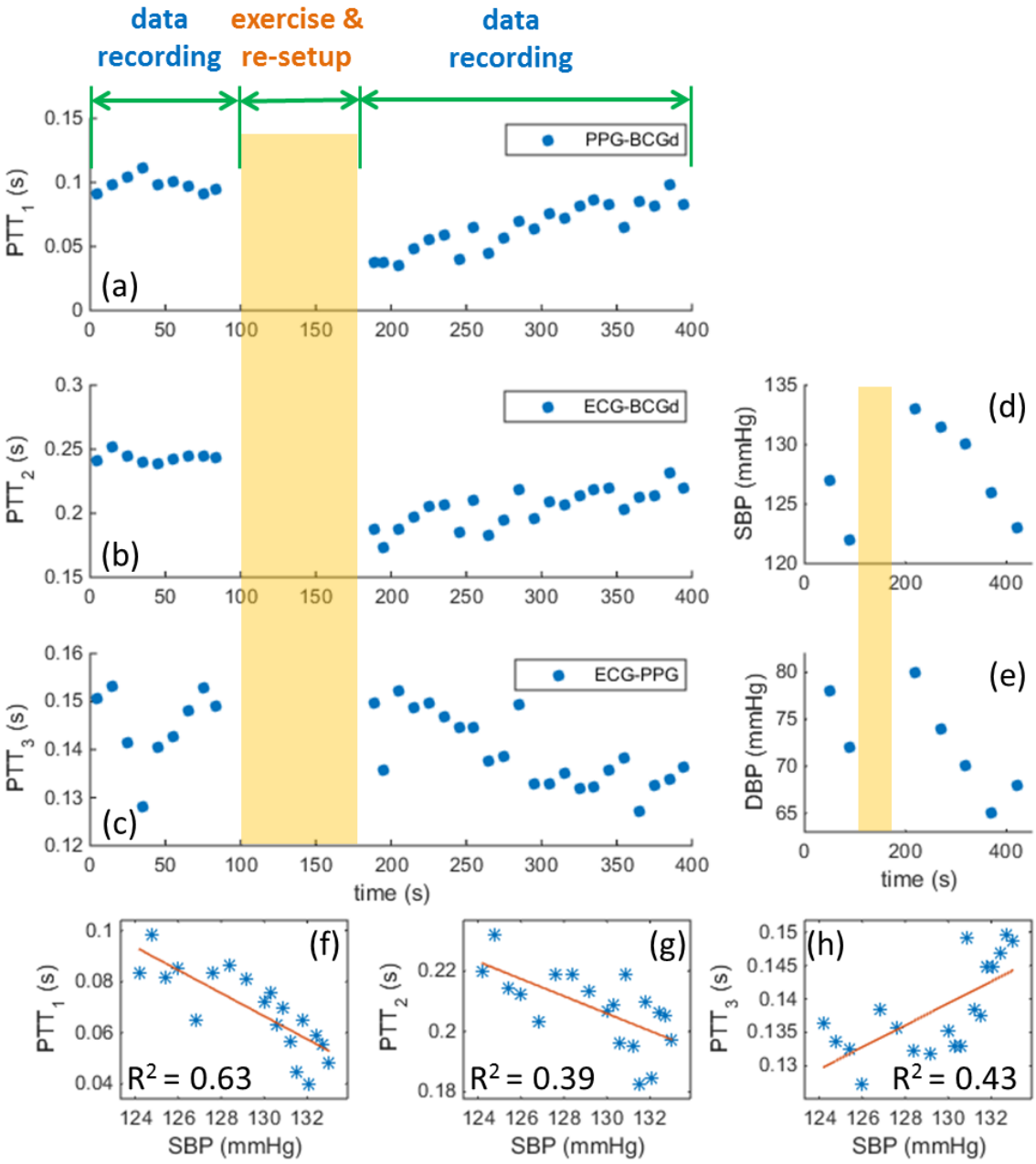

Figure 6-3 PTTs, BPs Tracking Results and Correlations (Subject #1).
(a-c) PTT values obtained from three methods. (d-e) Reference BP values. (f-h) Correlations between three PTT values and SBP. The red lines are linear fits.

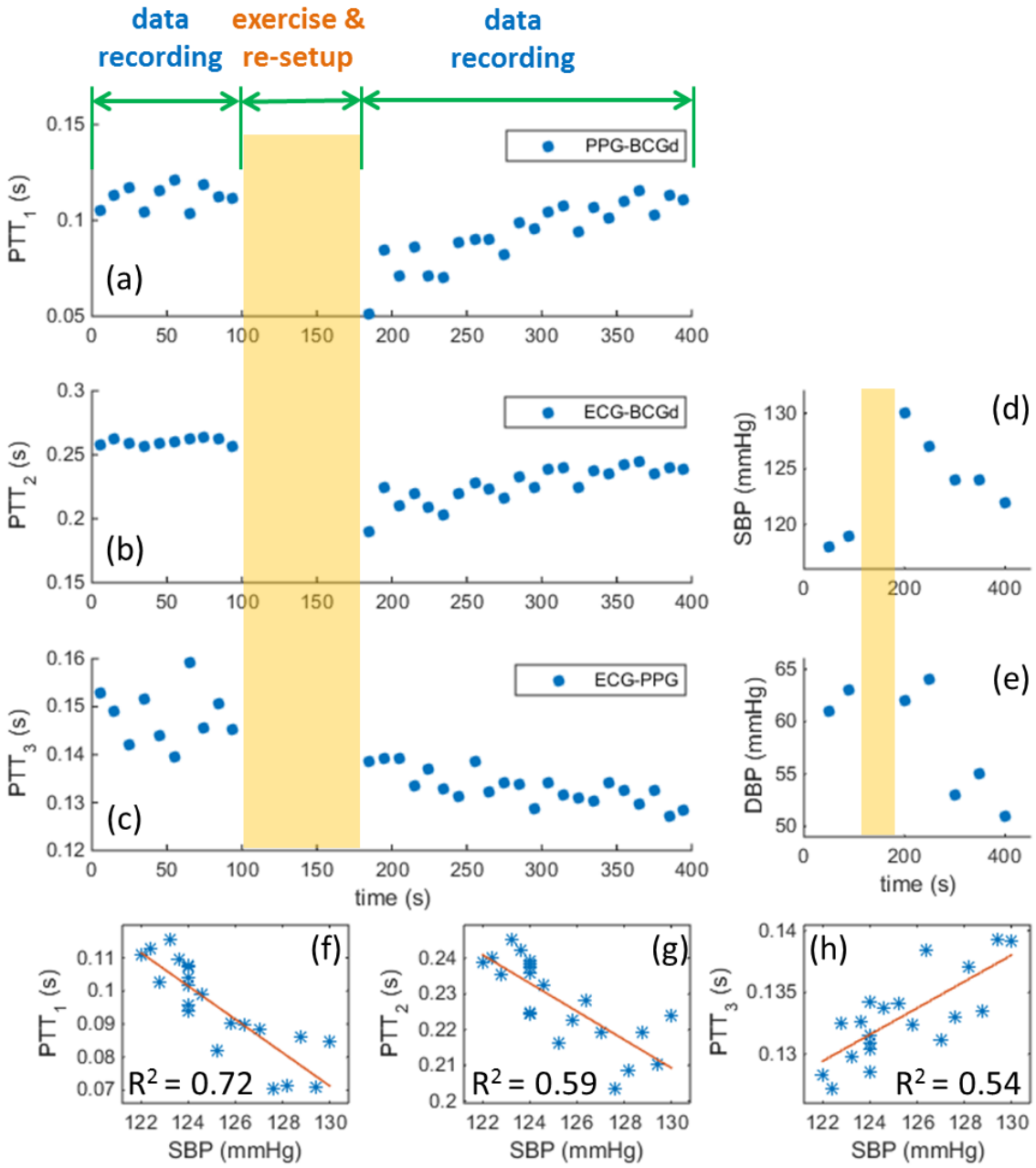

Figure 6-4 PTTs, BPs Tracking Results and Correlations (Subject #2).
(a-c) PTT values obtained from three methods. (d-e) Reference BP values. (f-h) Correlations between three PTT values and SBP. The red lines are linear fits.

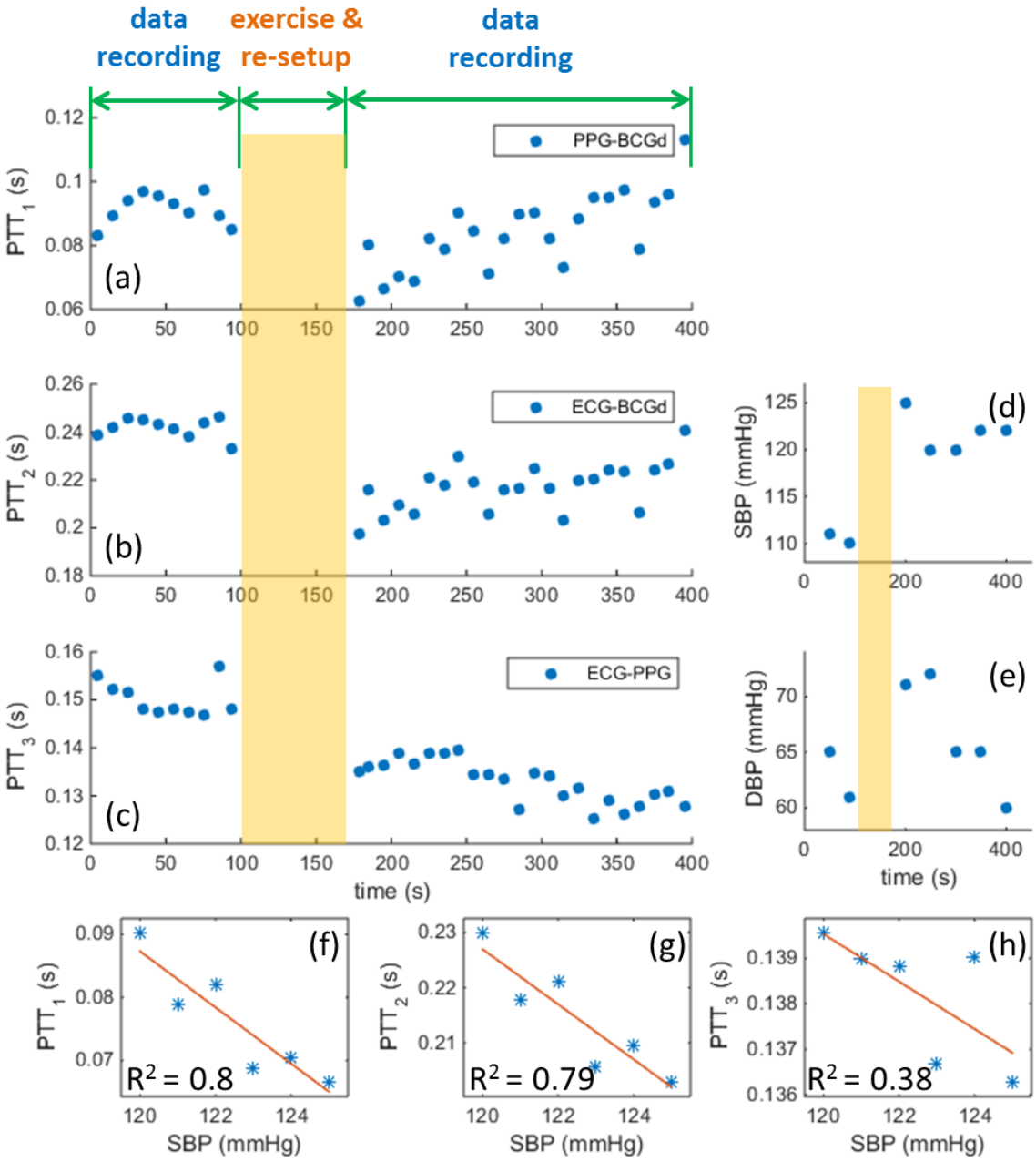

Figure 6-5 PTTs, BPs Tracking Results and Correlations (Subject #3).
(a-c) PTT values obtained from three methods. (d-e) Reference BP values. (f-h) Correlations between three PTT values and SBP. The red lines are linear fits.

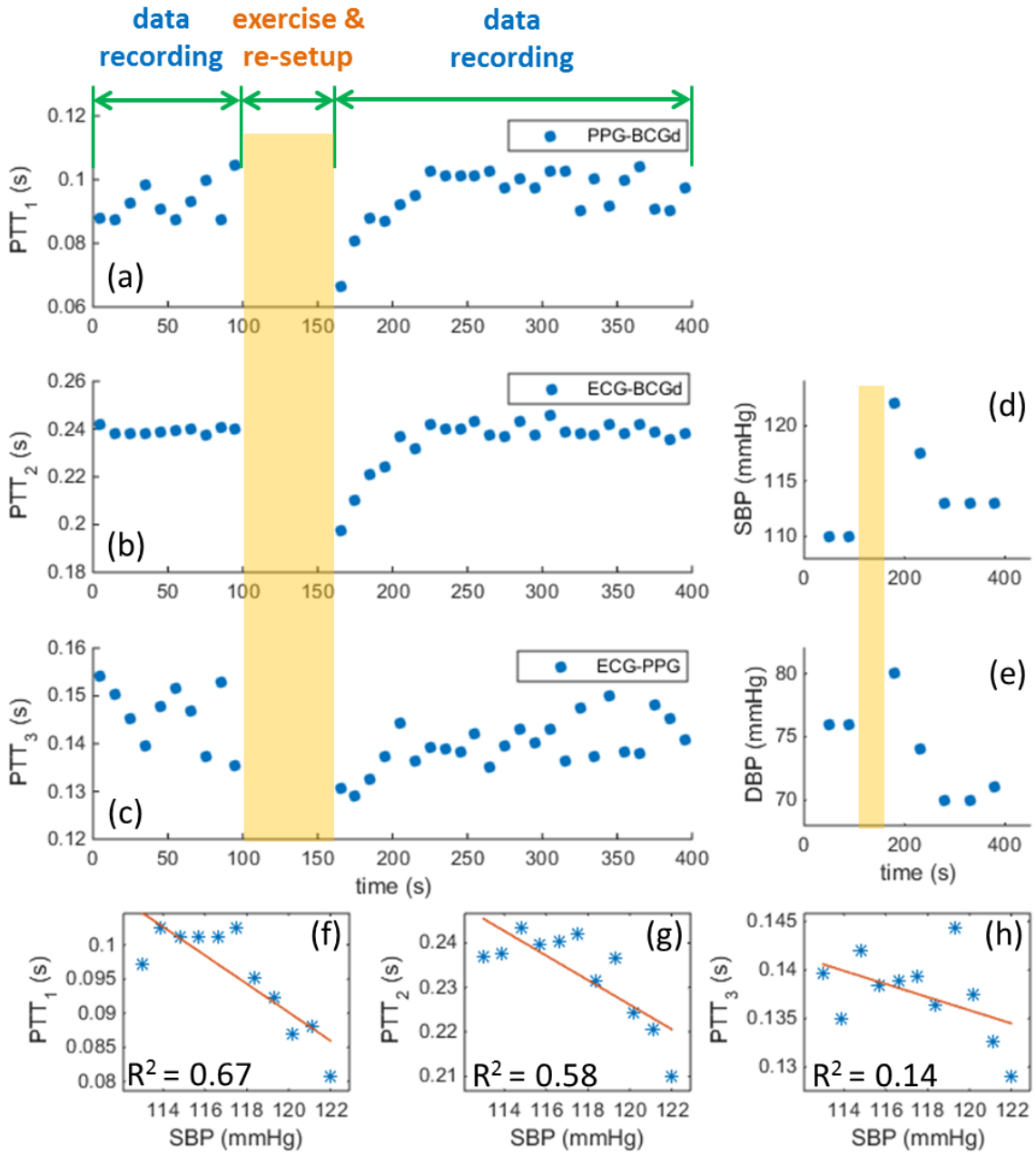

Figure 6-6 PTTs, BPs Tracking Results and Correlations (Subject #4).
(a-c) PTT values obtained from three methods. (d-e) Reference BP values. (f-h) Correlations between three PTT values and SBP. The red lines are linear fits.

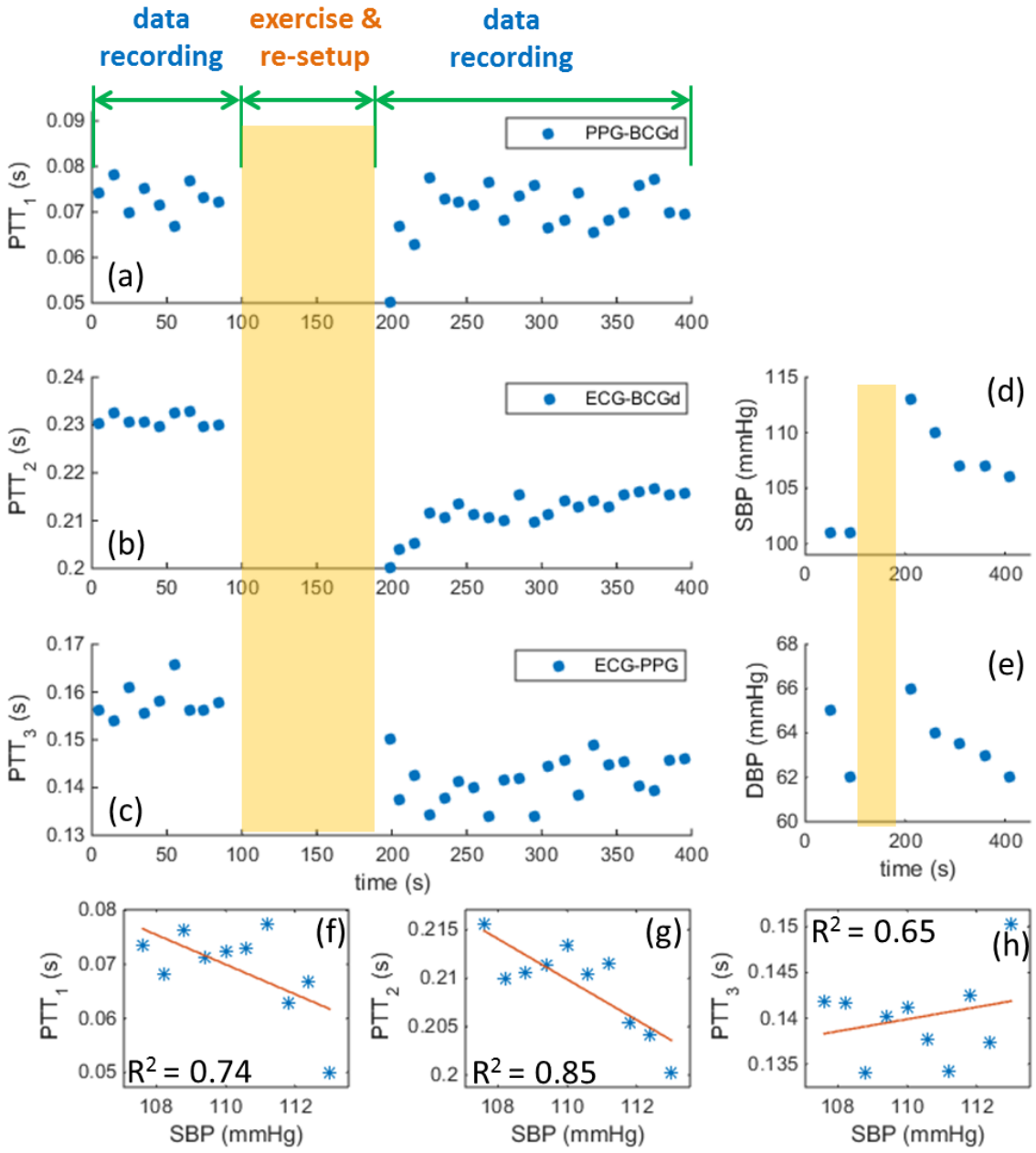

Figure 6-7 PTTs, BPs Tracking Results and Correlations (Subject #5).
(a-c) PTT values obtained from three methods. (d-e) Reference BP values. (f-h) Correlations between three PTT values and SBP. The red lines are linear fits.

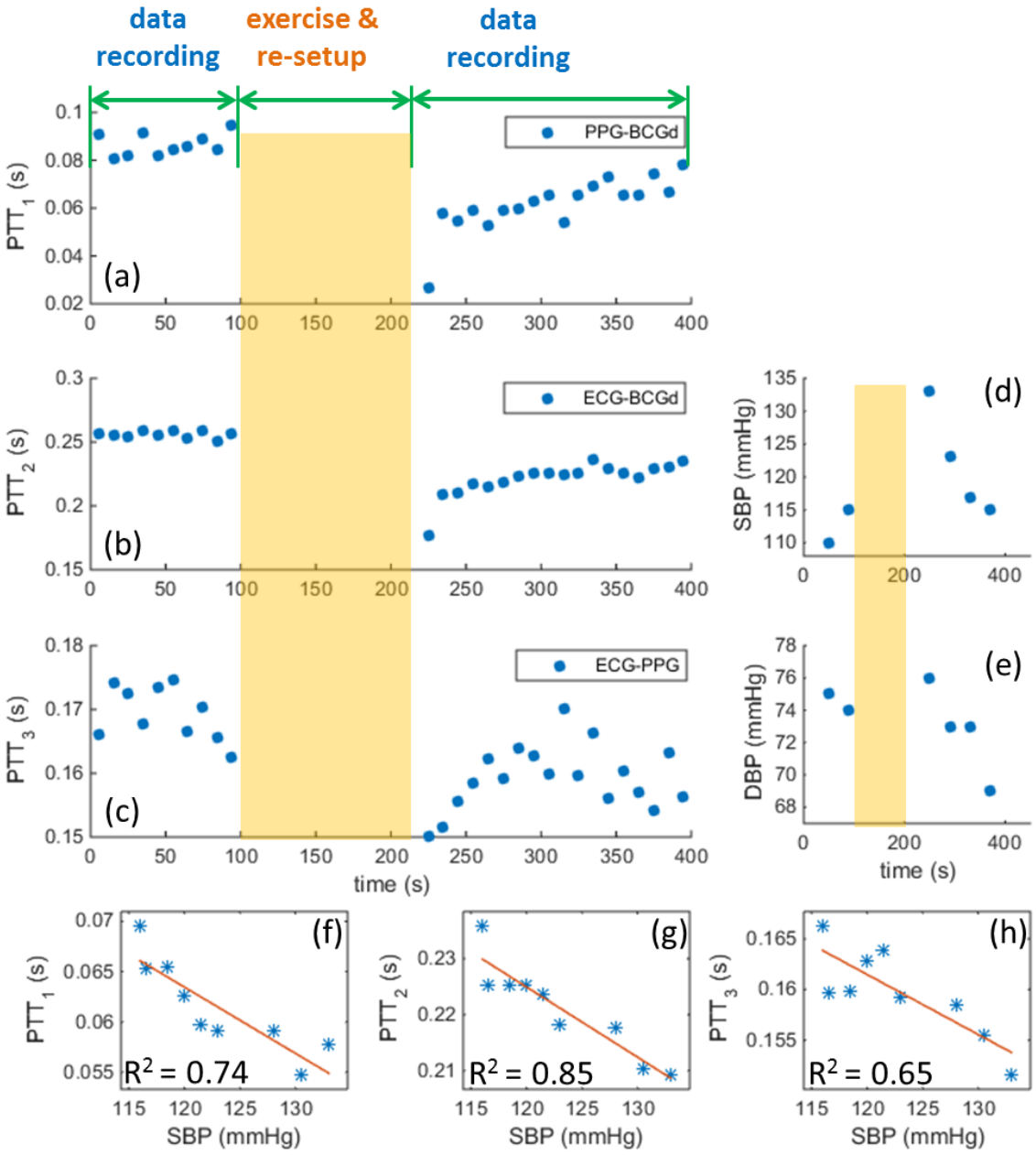

Figure 6-8 PTTs, BPs Tracking Results and Correlations (Subject #6).
(a-c) PTT values obtained from three methods. (d-e) Reference BP values. (f-h) Correlations between three PTT values and SBP. The red lines are linear fits.

With all the subjects, PTT_1 and PTT_2 show overall better correlations with BP compared with PTT_3. Relying completely on ECG may introduce variability in pre-ejection

period [83], and PPG at current state has considerable noise level. Combining these two factors together probably makes PTT_3 have the worst correlation with BP.

6.6 Detection of Premature Ventricular Contraction

During the experiment for BP monitoring, premature ventricular contraction (PVC) was also detected with both presented video-based method and reference ECG.

PVC is the extra, abnormal heartbeat that begins in one of the heart's two lower chambers. It is a sign of decreased oxygenation to the heart muscle. It occurs in most people at some point with the feeling as "skipped beats". Causes of PVC may include medications, alcohol, anxiety, and so on. For most people with isolated PVCs, treatment is not needed. However, if PVCs occur continuously for longer than 30 seconds, it may indicate serious cardiac condition.

Traditional method to diagnose PVC is based on ECG. PVC pattern can be easily distinguished from a normal heart beat. Normally, to detect PVC, the patients are required to wear a conventional Holter monitor to record ECG continuously for about 48 hours, and the data is saved and analyzed by doctors later. The electrodes of Holter monitor are attached to the patients' chest, resulting in discomfort and limitation of freedom. Other than ECG-based methods, researchers have also reported PVC detection based on PPG and BCG waveforms with contact-based methods. In PPG recorded by sensor attached to the finger, PVC can be recognized by an abnormal longer peak-peak interval [118]. Inan et al. detected PVC based on acceleration BCG using weighing scale by finding the significantly lower BCG "IJ" amplitudes.

During the experiment, the occurrences of PVC were found with one subject. The frequency of PVC appearance was about twice in five minutes. The PVC patterns can be recognized from both PPG and BCG waveforms and the happenings of PVC were also confirmed by the synchronized ECG recordings.

Figure 6-9 and Figure 6-10 show the occurrences of PVC with the same subject on different days. The shadowed areas indicate the occurrences of PVC. ECG, PPG, and BCG waveforms were recording simultaneously. In ECG (Figure 6-9 (a) and Figure 6-10 (a)), the abnormal forms of PVC were found in QRS-complex. In PPG (Figure 6-9 (b) and Figure 6-10 (b)), longer peak-peak intervals were found. In displacement BCG (Figure 6-9 (c) and Figure 6-10 (c)), J_d peaks showed lower amplitudes and the whole cycles looked incomplete compared with regular heartbeat cycles. In acceleration BCG (Figure 6-9 (d) and Figure 6-10 (d)), the "IJ" amplitudes of PVC were lower than those in neighboring normal heartbeat cycles.

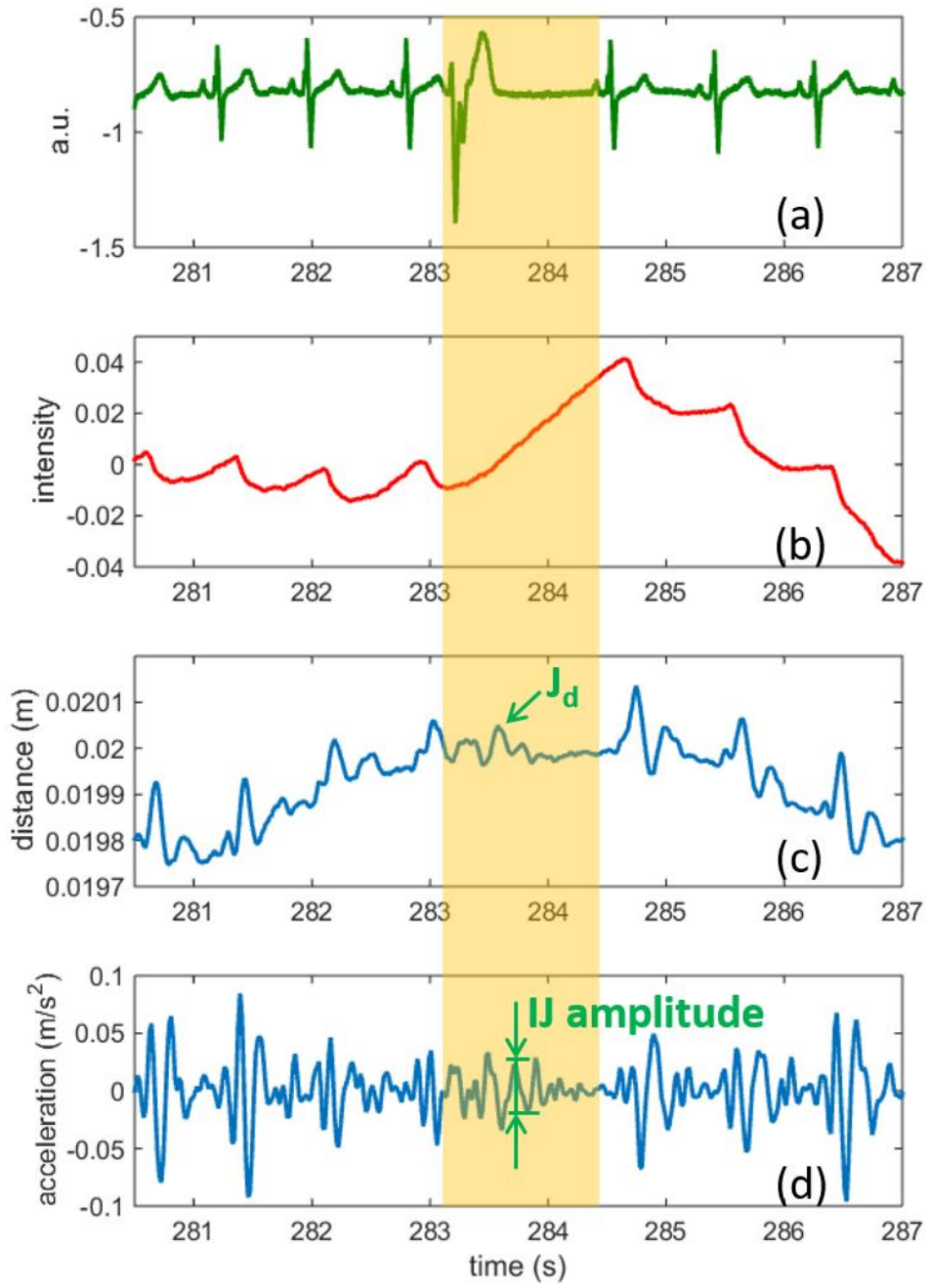

Figure 6-9 Occurrence of PVC in Different Cardiac Signals.
(a) ECG. (b) PPG. (c) Displacement BCG. (d) Acceleration BCG. Shadowed areas indicate the occurrence of PVC.

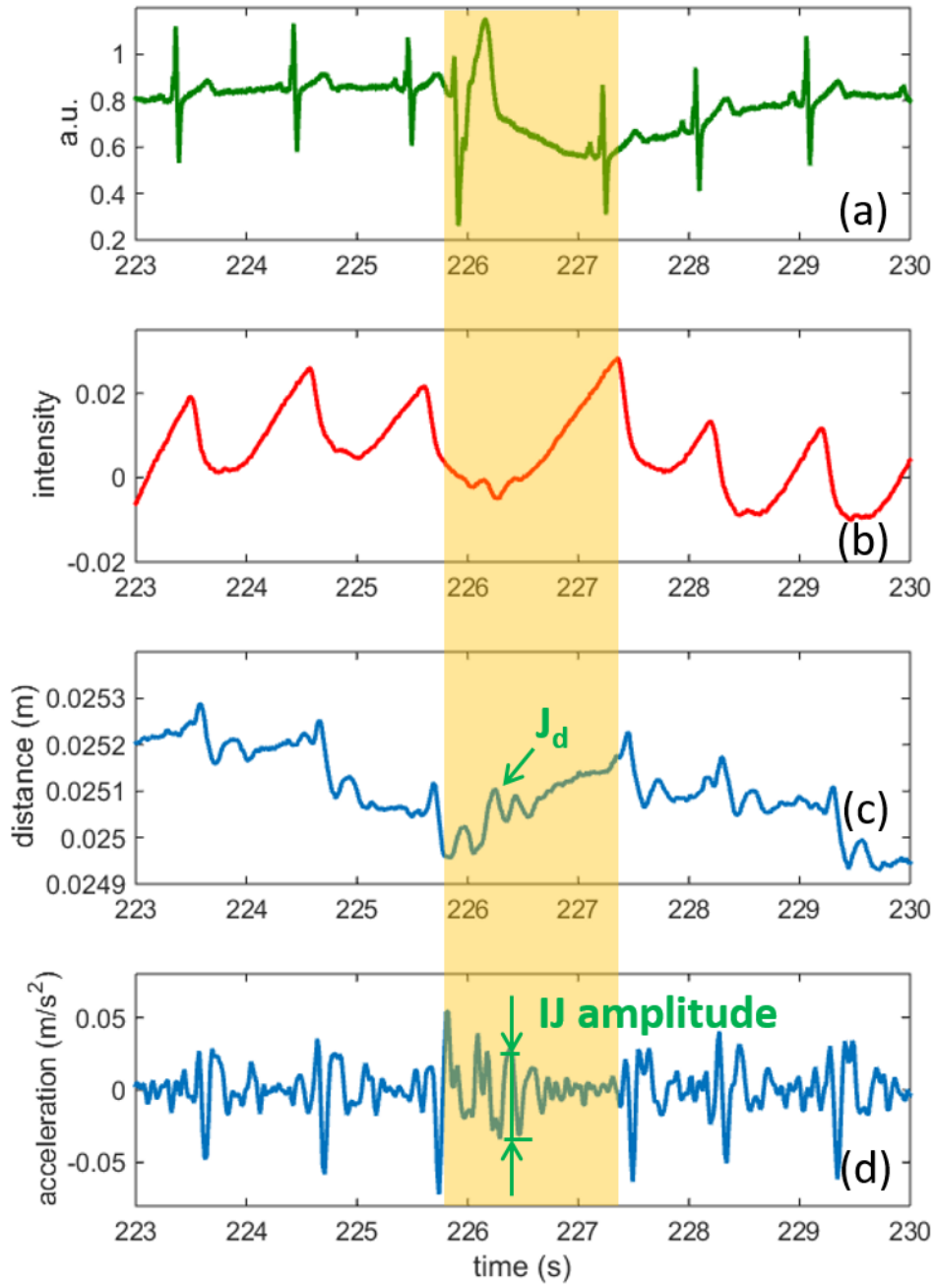

Figure 6-10 Occurrence of PVC with the Same Subject in Another Day.
(a) ECG. (b) PPG. (c) Displacement BCG. (d) Acceleration BCG. Shadowed areas indicate the occurrence of PVC.

6.7 Discussion

For the blood pressure experiment, the subjects were asked to exercise to change their blood pressure. Exercise makes muscles consume more oxygen. As a result, the heart pumps more blood around the body together with more powerful contractions which increases the blood pressure. However, exercise may introduce extra body motions which influence the PPG and BCG qualities, especially for BCG, which is a recording of small body movement. New test protocols may be needed to validate presented method without introduction of extra motion artifacts. One of the potential solutions is using medicine (e.g. Nitroglycerin), which will change blood pressure without extra body movements. However, the implementation of this protocol may need collaboration with professional medical staff.

Individual calibration is a limitation of blood pressure monitoring using PTT method, which is due to the mechanical properties of an individual's vascular wall and other factors [106]. Currently, PTT-based methods have been proven to track the trend of blood pressure change especially for SBP, however, getting absolute blood pressure values without calibration is difficult to achieve.

Using video-based technique potentially can potentially provide a non-contact solution for long term PVC monitoring. A better understanding of PVC patterns in PPG and BCG may help automate recognition of such events.

CHAPTER 7

CONCLUSIONS AND PERSPECTIVE

In summary, this work presented non-contact methods to monitor multiple physiological signals through the use of camera. By implementing different algorithms, different physiological waveforms were obtained, based on which, vital signs were further extracted. The major contributions of this work include:

1) A PPG detection system in ambient light condition, which can measure not only heart rate, but also PTT from two PPG waveforms at different body sites.

2) A dual-wavelength illumination system with triggered-camera control, which can measure SpO_2.

3) A respiration monitoring platform based on differential image processing, from which respiration rate and exhalation flow rate can be estimated.

4) A BCG detection method based on facial feature motion tracking.

5) A blood pressure tracking method based on PTT analysis from PPG and BCG waveforms, both of which are obtained from the same body location with one video clip.

6) As a byproduct of the experiment, PVC patterns can also be measured from acquired waveforms, either PPG or BCG, from video data.

Subject tests have been carried out as preliminary studies to validate these developed methods and applications.

There are some limitations and issues associated with the presented work:

1) For some of the measurements, like exhalation flow rate, SpO_2 and blood pressure, individual calibration is needed for each subject. The lack of a general calibration solution limits the practicality of the presented method.

2) Faster frame rate is always preferable to achieve higher temporal resolution for aforementioned waveforms. The fastest frame rate that can be reached based on the current equipment settings is 120 frames/second (with Pike camera). If faster frame rate can be obtained by using more advanced hardware resource, it will be beneficial for analyzing the high frequency features and timing characteristics of the signals.

3) In some of the measurements, due to resource limitation, the reference technologies are not the best options. For example, CO-oximeter will be more accurate to calibrate the presented SpO_2 measurement platform than the reference device used in this work, which is a commercial pulse oximeter. For BP measurement, a real-time BP monitor will also be a better choice than the cuff-based BP monitor used for reference, since the former one could provide beat-to-beat measurement of BP, which may help in obtaining a better correlation between the PTT values measured using the presented method and the absolute BP values.

4) Since all of these signals are sensitive to motion-induced artifacts, an effective tracking algorithm may help mitigate noise due to unwanted body motions. Accurate recording of these physiological signals may help better interpret the corresponding waveforms for further applications. In this work, only phase correlation method is used. Although it can help correct some of the motion artifacts, in some cases, when the motion is intense or has similar frequency range as the physiological signals of interest, its

performance is not satisfactory. Researchers have reported their efforts on this topic [20, 119], and while their methods are effective under certain circumstances, a more generic and comprehensive solution is still lacking.

5) For the pilot studies in the presented work, almost all of the subjects were young and healthy. If clinical study could be conducted with population with abnormal cardiovascular functions, it might be helpful to find the physiological relevance between the obtained waveform features and related disease symptoms, which can further validate the clinical values of the presented techniques.

If these issues were to be addressed in the future, the presented method could be further improved.

A potential application model based on the presented work can be an integrated physiological measurement platform intended for use in daily life as an extension of professional medical equipment that are normally hard to employ in home environment. Continuation of miniaturization, improvements in power dissipation, data transmission and overall camera optics at a pace similar to that seen in the past few years, will make the camera-based methods easier to implement and operate, which could provide convenient and low-cost medical measurements and health tracking solutions for all of the population.

REFERENCES

[1] S. Yu and J. Cheng, "A wireless physiological signal monitoring system with integrated Bluetooth and WiFi technologies," in *Proc. IEEE Eng. Med. Biol. Soc.*, Shanghai, China, 2005, pp. 2203-2206.

[2] R. Paradiso, "Wearable health care system for vital signs monitoring," in *Proc. IEEE Conference on Information Technology Applications in Biomedicine*, Prato, Italy, 2003, pp. 283-286.

[3] C. G. Scully, J. Lee, J. Meyer, A. M. Gorbach, D. Granquist-Fraser and Y. Mendelson, "Physiological parameter monitoring from optical recordings with a mobile phone," *IEEE Trans. Biomed. Eng.*, vol. 59, no. 2, pp. 303-306, Feb. 2012.

[4] B. Won and H. Park, "A touchscreen as a biomolecule detection platform," *Angew. Chem. Int. Ed.*, vol. 51, no. 3, pp. 748-751, Jan. 2012.

[5] C. C. Y. Poon, Q. Liu, H. Gao, W. Lin and Y. Zhang, "Wearable intelligent systems for E-Health," *JCSE*, vol. 5, no. 3, pp. 246-256, Sep. 2011.

[6] V. Chandrasekaran, "Measuring vital signs using smart phones," M.S. thesis, Dept. Computer Science, Univ. of North Texas, Denton, TX, pp. 6-16, 2010.

[7] J. Pickett, P. Amoroso, D. V. Nield and D. P. Jones, "Pulse oximetry and PPG measurements in plastic surgery," in *Proc. IEEE Int. Conf. EMBS*, Chicago, USA, 1997, vol. 5, pp. 2330-2332.

[8] P. K. Baheti and H. Garudadri, "An ultra low power pulse oximeter sensor based on compressed sensing," in *6th Intl. Workshop on Wearable and Implantable Body Sensor Networks*, Berkeley, USA, Jun. 2009, pp. 144-148.

[9] M. Garbey, N. Sun, A. Merla and I. Pavlidis, "Contact-free measurement of cardiac pulse based on the analysis of thermal imagery," *IEEE Trans. Biomed. Eng.*, vol. 54, no.8, 1418-1426, Aug. 2007.

[10] W. Verkruysse, L. O. Svaasand, and J. S. Nelson, "Remote plethysmographic imaging using ambient light," *Opt. Exp.*, vol. 16, no. 26, pp. 21434-21445, Dec. 2008.

[11] C. Takano and Y. Ohta, "Heart rate measurement based on a time-lapse image," *Med. Eng. Phys.*, vol. 29, no. 8, pp. 853-857, Oct. 2006.

[12] S. Hu, J. Zheng, V. Chouliaras and R. Summers, “Feasibility of imaging photoplethysmography,”on *Proc. Int. Conf. on BMEI*, Sanya, China, May. 2008, pp. 72-75.

[13] Y. Sun, S. Hu, V. Azorin-Peris, R. Kalawsky and S. Greenwald, “Noncontact imaging photoplethysmography to effectively access pulse rate variability,” *J. Biomed. Opt.*, vol. 18, no. 6, Jun. 2013.

[14] D. Shao et al., “Noncontact monitoring breathing pattern, exhalation flow rate and pulse transit time,” *IEEE Trans. Biomed. Eng.*, vol. 61, no. 11, pp. 2760-2767, Nov. 2014.

[15] G. Lempe, S. Zaunseder, T. Landgraf and H. Malberg, “ROI selection for remote photoplethysmography”, in *Proc. Workshop Bildverarbeitung für die Medizin*, Heidelberg, Germany, 2013, pp. 99-103.

[16] F. P. Wieringa, F. Mastik, and A. F. W. Van der Steen, “Contactless multiple wavelength photoplethysmographic imaging: a first step toward ‘SpO_2 camera’ technology,” *Ann. Biomed. Eng.*, vol. 33, no. 8, pp. 1034-1041, 2005.

[17] S. Kwon, H. Kim and K. S. Park, “Validation of heart rate extraction using video imaging on a built-in camera system of a smartphone,” in *Proc. IEEE Ann. Int. Conf. on EMBC*, Seoul, South Korea, Aug.28-Sep.1, 2012, pp. 2174-2177.

[18] M. Z. Poh, D. J. McDuff and R. W. Picard, “Non-contact, automated cardiac pulse measurements using video imaging and blind source separation,” *Opt. Expr.*, vol. 18, no. 10, pp. 10762-10774, May 2010.

[19] M. Z. Poh, D. J. McDuff and R. W. Picard, “Advancements in noncontact, multiparameter physiological measurements using a webcam,” *IEEE Trans. Biomed. Eng.*, vol. 58, no. 1, pp. 7-306, Jan. 2011.

[20] G. de Hann et al., “Robust pulse rate from chrominance-based rPPG,” *IEEE Trans. Biomed. Eng.*, vol. 60, no. 10, pp. 2878-2886, Oct. 2013.

[21] D. McDuff et al., “Remote measurement of cognitive stress via heart rate variability”, in *Proc. IEEE Eng. Med. Biol. Soc.*, Chicago, Illinois, USA, 2014, pp. 2957-2960.

[22] D. Shao et al., “Noncontact monitoring of blood oxygen saturation using camera and dual-wavelength imaging system,” *IEEE Trans. Biomed. Eng.*, vol. 63, no. 6, pp. 1091-1098, Jun. 2016.

[23] C. S. Kim et al., “Ballistocardiogram as Proximal Timing Reference for Pulse Transit Time Measurement: Potential for Cuffless Blood Pressure Monitoring”, *IEEE Trans. Biomed. Eng.*, vol. 62, no. 11, pp. 2657-2664, Nov. 2015.

[24] H. Gesche et al., “Continuous blood pressure measurement by using the pulse transit time: comparison to a cuff-based method,” *Eur. J. Appl. Physiol.*, vol. 112, no. 1, pp. 309-315, Jan. 2012.

[25] A. Reisner, P. Shaltis, D. McCombie and H. Asada, “Utility of the photoplethysmogram in circulatory monitoring,” *Anesthesiology*, vol. 108, no. 5, pp. 950-958, May 2008.

[26] M. Nitzan, B. Khanokh and Y. Slovik, “The difference in pulse transit time to the toe and finger measured by photoplethysmography,” *Physiol. Meas.*, vol. 23, no. 1, pp. 85-93, Feb. 2002.

[27] P. Boutouyrie, M. Briet, C. Collin, S. Vermeersch, and B. Pannier, “Assessment of pulse wave velocity,” *Artery Research*, vol. 3, no. 1, pp. 3-8, Dec. 2008.

[28] J. C. Bramwell and A. V. Hill, “Velocity of transmission of the pulse-wave and elasticity of arteries,” *The Lancet*, vol. 199, no. 5149, pp. 891-892, May 1922.

[29] S. I. Rabben, N. Stergiopulos, L. R. Hellevik, O. A. Smiseth, S. Slordahl, S. Urheim and B. Angelsen, “An ultrasound-based method for determining pulse wave velocity in superficial arteries,” *J. Biomech.*, vol. 37, no. 10, pp. 1615-1622, Oct. 2004.

[30] P. J. Brands, J. M. Willigers, L. A. F. Ledoux, R. S. Reneman and A. P.G. Hoeks, “A noninvasive method to estimate pulse wave velocity in arteries locally by means of ultrasound,” *Ultrasound Med. Biol.*, vol. 24, no. 9, pp. 1325-1335, Nov. 1998.

[31] J. R. Jago and A. Murray, “Repeatability of peripheral pulse measurements on ears, fingers and toes using photoelectric plethysmography,” *Clin. Phys. Physiol. Meas.*, vol. 9, no. 4, pp. 319-329, Nov. 1988.

[32] J. Allen and A. Murray, “Age-related changes in peripheral pulse timing characteristics at the ears, fingers and toes,” *Physiol. Meas.*, vol. 16, no. 10, pp. 711-717, Oct. 2002.

[33] C. D. Maria et al., “Feasibility of monitoring vascular ageing by multi-site photoplethysmography,” in *Proc. Computing in Cardiology*, Krakow, Poland, 2012, pp. 817-820.

[34] A. Babchenko, E. Davidson, D. Adler, Y. Ginosar, V. Kurz and M. Nitzan, "Increase in pulse transit time to the foot after epidural anaesthesia treatment," *Med. Bio. Eng. Comput.*, vol. 38, no. 6, pp. 674-679, Nov. 2000.

[35] M. Tavakoli, L. Turicchia, and R. Sarpeshkar, "An ultra-low-power pulse oximeter implemented with an energy-efficient transimpedance amplifier," *IEEE Trans. Biomed. Circuits Syst.*, vol. 4, no. 1, pp. 27-38, 2010.

[36] " Understanding Continuous Mixed Venous Oxygen Saturation (SvO_2) Monitoring with the Swan–Ganz Oximetry TD System", Edwards Lifesciences LLC, 2002, pp. 1.

[37] Withings, "What does SpO_2 mean? What is the normal blood oxygen level?" Available: https://withings.zendesk.com/hc/en-us/articles/201494667-What-does-SpO2-mean-What-is-the-normal-blood-oxygen-level-.

[38] V. Kamat, "Pulse oximetry," *Indian J. Anaesth.*, vol. 46, no.4, pp. 261-268, 2002.

[39] P. E. Bickler, J. R. Feiner, and J.W. Severinghaus, "Effects of skin pigmentation on pulse oximeter accuracy at low saturation," *Anesthesiology*, vol. 102, no. 4, pp. 715-719, 2005.

[40] K. Humphreys, T. Ward, and C. Markham. "A CMOS camera-based pulse oximetry imaging system," in *Proc. IEEE Eng. Med. Biol. Soc.*, Shanghai, China, vol. 4, 2005, pp. 3494-3497.

[41] K. Humphreys, T. Ward, and C. Markham, "Noncontact simultaneous dual wavelength photoplethysmography: A further step toward noncontact pulse oximetry," *Rev. Sci. Instrum.*, vol. 78, no. 4, pp. 044304, 2007.

[42] L. Kong et al., "Non-contact detection of oxygen saturation based on visible light imaging device using ambient light," *Opt. Exp.*, vol. 21, no. 15, pp. 17464-17471, 2013.

[43] L. Tarassenko et al., "Non-contact video-based vital sign monitoring using ambient light and auto-regressive models," *Physiol. Meas.*, vol. 35, no. 5, pp. 807-831, 2014.

[44] U. Bal, "Non-contact estimation of heart rate and oxygen saturation using ambient light," *Biomed. Opt. Exp.*, vol. 6, no. 1, pp. 86-97, Dec. 2014.

[45] U. S. Freitas, "Remote Camera-based Pulse Oximetry," in *Proc. The Sixth International Conference on eHealth, Telemedicine, and Social Medicine*, Barcelona, Spain, 2014, pp. 59-63.

[46] J. Lee et al., “Comparison between red, green and blue light reflection photoplethysmography for heart rate monitoring during motion,” in *Proc. IEEE Eng. Med. Biol. Soc.*, Osaka, Japan, 2013, pp. 1724-1727.

[47] J. Jiang et al., “What is the space of spectral sensitivity functions for digital color cameras?” in *Proc. Workshop on Appl. Comput. Vis.*, 2013, pp. 168-179.

[48] H.-Y., Tsai et al., “A study on oxygen saturation images constructed from the skin tissue of human hand,” in *Proc. IEEE Int. Instrum. Meas. Technol. Conf.*, Minneapolis, Minnesota, USA, May 2013, pp. 58-62.

[49] H.-Y., Tsai et al., “A Noncontact Skin Oxygen-Saturation Imaging System for Measuring Human Tissue Oxygen Saturation,” *IEEE Trans. Instrum. Meas.*, vol. 63, no. 11, pp. 2620-2631, Nov. 2014.

[50] S. Prahl, “Optical absorption of hemoglobin,” Oregon Medical Laser Center, Portland, OR, USA, Available: http://omlc.org/spectra/hemoglobin/summary.html.

[51] G. M. Azmal, A. Al-Jumaily, and M. Al-Jaafreh, “Continuous measurement of oxygen saturation level using photoplethysmography signal,” in *Proc. IEEE ICBPE*, Singapore, 2006, pp. 504-507.

[52] L. F. C. Martinez, L.F., G. Paez, and M. Strojnik, “Optimal wavelength selection for noncontact reflection photoplethysmography,” in *Proc. 22nd Congress of the International Commission for Optics*, Nov. 2011.

[53] W. S. Johnston, “Development of a signal processing library for extraction of SpO_2, HR, HRV, and RR from photoplethysmographic waveforms,” M.S. thesis, Dept. Biomed. Eng.2006, Worcester Polytechnic Institute, Worcester, MN, USA, 2006.

[54] T. L. Rusch, R. Sankar, and J. E. Scharf, “Signal processing methods for pulse oximetry,” *Comput. Biol. Med.*, vol. 26, no. 2, pp. 143-159, 1996.

[55] J. E. Scharf and T. L. Rusch, "Optimization of portable pulse oximetry through Fourier analysis," in *Proc. IEEE SBEC*, Apr. 1993.

[56] T. L. Rusch, R. Sankar, and J. E. Scharf, “Signal processing methods for pulse oximetry,” *Comput. Biol. Med.*, vol. 26, no. 2, pp. 143-159, 1996.

[57] J. M. Kim et al., “Signal processing using Fourier & wavelet transform for pulse oximetry,” in *Proc. CLEO*, Chiba, Japan, 2001, vol. 2, pp. 310-311.

[58] J. E. Scharf, S. Athan, and D. Cain, "Pulse oximetry through spectral analysis," in *Proc. IEEE SBEC*, Apr. 1993.

[59] Y. Sun et al., “Motion-compensated noncontact imaging photoplethysmography to monitor cardiorespiratory status during exercise,” *J. Biomed. Opt.*, vol. 16, no. 7, pp. 077010, 2011.

[60] L. Feng et al., “Motion-Resistant Remote Imaging Photoplethysmography Based on the Optical Properties of Skin,” *IEEE Trans. Circuits Syst. Video Technol.*, vol. 25, no. 5, pp. 879-891, May. 2015.

[61] J. G. Webster, *Design of Pulse Oximeters.* Institute of Physics Publishing, UK, 1997.

[62] I. Fine, A. Weinreb, “Multiple scattering effect in transmission pulse oximetry”, *Med. Biol. Eng. Comput.*, vol. 33, no. 5, pp. 709-712, Sep. 1995.

[63] G. Zonios, U. Shankar, and V. K. Iyer, “Pulse Oximetry Theory and Calibration for Low Saturations”, *IEEE Trans. Biomed. Eng.*, vol. 51, no. 5, pp.818-822, May 2004.

[64] F. Zhao, M. Li, Y. Qian and J. Z. Tsien, “Remote measurements of heart and respiration rates for telemedicine,” *PLOS ONE*, vol. 8, no. 10, Oct. 2013.

[65] S. Jin and G. Koh, “A robust image tracker based on phase correlation and fourier-mallin transform,”on *Proc. Int. Conf. on ICCAS*, Seoul, Korea, Oct. 2008, pp. 1028-1031.

[66] I. Starr, “On reading ballistocardiograms,” *Am. J. Cardiol.*, vol. 2, no. 4, pp. 404-416, Oct. 1958.

[67] I. Starr, “Essay on the ballistocardiogram,” *J. AM. Med. Assoc.*, vol. 155, no. 16, pp. 1413-1425, Aug. 1954.

[68] I. Starr, “Normal standards for amplitude of ballistocardiograms calibrated by force,” *Circulation*, vol. 11, no. 6, pp. 914-926, Jun. 1955.

[69] D. H. Jackson et al., “Ballistocardiographic and angiographic correlation study in idiopathic hypertrophic subaortic stenosis,” *Bibl. Cardiol.*, vol. 27, pp. 14-20, Jan. 1971.

[70] W. Goedhard, “Ballistocardiography: past, present and future,” *Bibl. Cardiol.*, vol. 37, pp. 27-45, 1978.

[71] I. Starr et al., “Twenty-year studies with the Ballistocardiograph”, *Circulation*, vol. 23, no. 5, pp. 714-732, May 1961.

[72] W. B. Thompson et al., "Ballistocardiography. II. The normal ballistocardiogram," *Circulation*, vol. 7, no. 3, pp. 321-328, Mar. 1953.

[73] L. Giovangrandi et al., "Ballistocardiography—a method worth revisiting," in *Proc. IEEE Eng. Med. Biol. Soc.*, Boston, Massachusetts, USA, 2011, pp. 4279-4282.

[74] D. He et al., "An ear-worn vital signs monitor," *IEEE Trans. Biomed. Eng.*, vol. 62, no. 11, pp. 2547-2552, Oct. 2015.

[75] A. G. W. van Brummelen et al., "On the elimination of pulse wave velocity in stroke volume determination from the ultralow-frequency displacement ballistocardiogram," *Am. Heart J.*, vol. 67, no. 3, pp. 374-378, Mar. 1964.

[76] I. Starr et al., "Studies on the estimation of cardiac output in man, and of abnormalities in cardiac function, from the heart's recoil and the blood's impacts; the ballistocardiogram," *Am. J. Physiol.*, vol. 127, no. 1, pp. 1-28, Aug. 1939.

[77] I. Starr et al., "Ballistocardiogram. II. Normal standards, abnormalities commonly found in diseases of the heart and circulation, and their significance," *J. Clin. Invest.*, vol. 19, no. 3, pp. 437-450, May 1940.

[78] W. R. Scarborough et al., "Proposals for ballistocardiographic nomenclature and conventions: revised and extended report of committee on ballistocardiographic terminology," *Circulation*, vol. 14, no. 3, pp. 435-450, Sep. 1956.

[79] I. Starr, "Progress towards a physiological cardiology: a second essay on the ballistocardiogram," *Ann. Intern. Med.*, vol. 63, no. 6, pp. 1079-1105, Dec. 1965.

[80] N. K. Corp. Half a century of contributing to medical care and society. [Online]. Available: http://www.nihonkohden.com/company/history/ 1950s.html.

[81] R. V. Elliott et al., "Acceleration ballistocardiography design, construction, and application of a new instrument," *Circulation*, vol. 9, no. 2, pp. 281-291, Feb. 1954.

[82] D. He et al., "A continuous, wearable, and wireless heart monitor using head ballistocardiogram (BCG) and head electrocardiogram (ECG)," in *Proc. IEEE Eng. Med. Biol. Soc.*, Boston, Massachusetts, 2011, pp. 4729-4732.

[83] E. S. Winokur et al., "A wearable vital signs monitor at the ear for continuous heart rate and Pulse Transit Time measurements," in *Proc. IEEE Eng. Med. Biol. Soc.*, San Diego, California, USA, 2012, pp. 2724-2727.

[84] D. He, "A wearable heart monitor at the ear using ballistocardiogram (BCG) and electrocardiogram (ECG) with a nanowatt ECG heartbeat detection circuit," Ph.D. dissertation, Electrical Engineering, Massachusetts Institute of Technology, Cambridge, Massachusetts, USA, 2013.

[85] O. T. Inan et al., "Robust ballistocardiogram acquisition for home monitoring," *Physiol. Meas.*, vol. 30, no. 2, pp. 169-185, Feb. 2009.

[86] J. H. Shin et al., "Non-constrained monitoring of systolic blood pressure on a weighing scale," *Physiol. Meas.*, vol. 30, no. 7, pp. 679-693, Jul. 2009.

[87] J. H. Shin et al., "HRV analysis and blood pressure monitoring on weighing scale using BCG," in *Proc. IEEE Eng. Med. Biol. Soc.*, San Diego, California, USA, 2012, pp. 3789-3792.

[88] J. Alametsä et al., "The potential of EMFi sensors in heart activity monitoring," in *Proc. 2nd OpenECG Workshop "Integration of the ECG into the HER & Interoperability of ECG Device Systems"*, Berlin, Germany, 2004.

[89] J. Alametsä et al., "Ballistocardiography in sitting and horizontal positions", *Physiol. Meas.*, vol. 29, no. 29, pp. 1071-1087, Aug. 2008.

[90] C. Brüser et al., "Adaptive beat-to-beat heart rate estimation in ballistocardiograms," *IEEE Trans. Inf. Technol. Biomed.*, vol. 15, no. 5, pp. 778-786, Sep. 2011.

[91] B. Ngai et al., "Comparative analysis of seismocardiogram waves with the ultra-low frequency ballistocardiogram," in *Proc. IEEE Eng. Med. Biol. Soc.*, Minneapolis, Minnesota, USA, 2009, pp. 2851-2854.

[92] J. W. Krug et al., "Optical ballistocardiography for gating and patient monitoring during MRI: an initial study," in *Proc. Computing in Cardiology Conference (CinC)*, Cambridge, Massachusetts, 2014, pp. 953-956.

[93] G. Balakrishnan et. al, "Detecting pulse from head motions in video," in *Proc. IEEE Computer Vision and Pattern Recognition (CVPR)*, Portland, Oregon, USA, 2013, pp. 3430-3437.

[94] J. Shi et al., "Good features to track," in *Proc. IEEE Computer Vision and Pattern Recognition (CVPR)*, Seattle, Washington, USA, 1994, pp. 593-600.

[95] C. Tomasi et al., "Detection and tracking of point features," Technical Report CMU-CS-91-132, Carnegie Mellon University, Pittsburgh, Pennsylvania, USA, 1991.

[96] B. Lucas et al., “An Iterative Image Registration Technique with an Application to Stereo Vision,” in *Proc. IJCAI*, Vancouver, British Columbia, Canada, 1981, pp. 674-679.

[97] R. Coppola et al., “Signal to noise ratio and response variability measurements in single trial evoked potentials”, *Electroencephalogr. Clin. Neurophysiol.*, vol. 44, no. 2, pp. 214-222, Feb. 1978.

[98] E. Pinheiro et al., “Theory and developments in an unobtrusive cardiovascular system representation: ballistocardiography,” *Open Biomed. Eng. J.*, vol. 4, pp. 201-216, Oct. 2010.

[99] P-F. Migeotte et al., “Three dimensional ballistocardiography: methodology and results from microgravity and dry immersion,” in *Proc. IEEE Eng. Med. Biol. Soc.*, Boston, Massachusetts, USA, 2011, pp. 4271-4274.

[100] S. Sachdeva, “Fitzpatrick skin typing: applications in dermatology,” *Indian J. Dermatol. Venereol. Leprol.*, vol. 75, no. 1, pp. 93-96, Jan-Feb. 2009.

[101] Y. Henderson, “The mass-movements of the circulation as shown by a recoil curve,” *Am. J. Physiol.*, vol. 14, pp. 287-298, Sep. 1905.

[102] W. R. Scarborough et al., “The nature of records from ultra-low frequency ballistocardiographic systems and their relation to circulatory events,” *Am. J. Cardiol.*, vol. 2, no. 5, pp. 613-641, Nov. 1958.

[103] P. A. Shaltis, A. T. Reisner, and H. H. Asada, "Cuffless blood pressure monitoring using hydrostatic pressure changes," *IEEE Trans. Biomed. Eng.*, vol. 55, no. 6, pp. 1775-1777, Jun. 2008.

[104] H. Asada, A. Reisner, P. Shaltis, and D. McCombie, "Towards the development of wearable blood pressure sensors: a photo-plethysmograph approach using conducting polymer actuators," in *Proc. IEEE Eng. Med. Biol. Soc.*, Shanghai, China, 2005, pp. 4156-4159.

[105] R. Mukkamala et al., "Towards ubiquitous blood pressure monitoring via pulse transit time: theory and practice," *IEEE Trans. Biomed. Eng.*, vol. 62, no. 8, pp. 1879-1901, Aug. 2015.

[106] A. Patzak, Y. Mendoza, H. Gesche, and M. Konermann, "Continuous blood pressure measurement using the pulse transit time: comparison to intra-arterial measurement," *Blood Press.*, vol. 24, no. 4, pp. 217-221, Apr. 2015.

[107] I. J. Vanderpohl, "Measuring multiple physiological parameters through blind signal processing of video parameters," U.S. Patent 20140275833 A1, Sep. 18, 2014.

[108] S. Stergiou, "Pulse wave transit time using two cameras as pulse sensors," U.S. Patent 20140043457, Feb. 13, 2014.

[109] E. Pinheiro, O. Postolache, and P. Girão, "Blood pressure and heart rate variabilities estimation using Ballistocardiography," in *Proc. the 7th Conf. on. Telecom.*, Santa Maria da Feira, Portugal, 2009, pp. 125-128.

[110] M. Etemadi, O. T. Inan, L. Giovangrandi, and G. T. A. Kovacs, "Rapid assessment of cardiac contractility on a home bathroom scale," *IEEE Trans. Inf. Technol. Biomed.*, vol. 15, no. 6, pp. 864-869, Nov. 2011.

[111] R. M. Wiard, L. B. Giovangrandi, and G. T. Kovacs, "Systems and methods for monitoring the circulatory system," U.S. Patent 20130310700 A1, Nov. 21, 2013.

[112] Z. Chen et al., "Noninvasive monitoring of blood pressure using optical Ballistocardiography and Photoplethysmograph approaches," in *Proc. IEEE Eng. Med. Biol. Soc.*, Osaka, Japan, 2013, pp. 2425-2428.

[113] Z. Chen et al., "Method and system for optical blood pressure monitoring," U.S. Patent 20150018637 A1, Jan. 15, 2015.

[114] L. Sherwood, "Biology, Human biology," in *Human Physiology, From Cells to Systems*. 8th ed., Cengage Learning, 2013.

[115] G. Langewouters, K. Wesseling, and W. Goedhard, "The static elastic properties of 45 human thoracic and 20 abdominal aortas in vitro and the parameters of a new model," *J. Biomech.*, vol. 17, no. 6, pp. 425-435, 1984.

[116] M. Y. M. Wong and Y. T. Zhang, "The relationship between pulse transit time and systolic blood pressure on individual subjects after exercises," in *Proc. D2H2*, Arlington, Virginia, USA, 2006, pp. 37-38.

[117] D. Shao, F. Tsow, C. Liu, Y. Yang, and N. Tao, "Simultaneous Monitoring of Ballistocardiogram and Photoplethysmogram Using Camera," *IEEE Trans. Biomed. Eng.*, to be published.

[118] A. Sološenko et al., "Photoplethysmography-based method for automatic detection of Premature Ventricular Contractions," *IEEE Trans. Biomed. Circuits Syst.*, vol. 9, no. 5, pp. 662-669, 2015.

[119] W. Wang, S. Stuijk, and G. de Haan, “Exploiting spatial-redundancy of image sensor for motion robust rPPG,” *IEEE Trans. Biomed. Eng.*, vol. 62, no. 2, pp. 415-425, Feb. 2015.